A STUDY OF DYNAMIC SIMILITUDE FOR MODELING STARTING JET VORTICES

A Thesis

by

ALEXANDER FREDDO

Submitted to the Office of Graduate and Professional Studies of
Texas A&M University
in partial fulfillment of the requirements for the degree of

MASTER OF SCIENCE

Chair of Committee,	Scott Socolofsky
Committee Members,	Kuang-An Chang
	Robert Hetland
Head of Department,	Sharath Girimaji

August 2019

Major Subject: Ocean Engineering

ABSTRACT

Accurate numerical simulations needed for responding to coastal oil spills require a fundamental understanding of tidal eddy-driven transport. Tidal eddies are commonly formed along barrier islands and shipping channels connecting bays/estuaries to the coast. The transport in and out of the bays/estuaries controlled by these eddies is critical for many barrier island coastlines across the United States. Understanding this major form of transport can assist response efforts to disasters, such as the Texas City Y spill. In this spill, a bulk carrier collided with an oil tanker spilling 168,000 gallons of oil in the Galveston Ship Channel and was eventually stranded along the coasts of Galveston and Matagorda island.

In order to improve the understanding of these tidal eddies, a shallow water flume was designed and constructed at Texas A&M University. This flume was designed based on the non-dimensional parameter space needed to describe the dynamic similitude of the behavior of coastal tidal eddies. The flume was then used to conduct surface particle image velocimetry (PIV) experiments for a 52.7 cm wide channel at 2cm, 3cm, and 5cm water depth, where the velocity information of the eddies was recorded during 5 to 10 tidal periods at different flow rates.

A method was developed for designing a shallow water flume within the critical parameter space needed for dynamic and geometric similitude. The newly designed flume was then tested and the hydrodynamic conditions present for the new design were analyzed and recorded for use in future experimentation. Experiments were conducted with similar parameters to other relevant research on shallow water starting jet vortices in larger facilities to compare the results of the design process to existing data sets. The results confirm that the present experiments give dynamically similar results.

ACKNOWLEDGMENTS

CONTRIBUTORS AND FUNDING SOURCES

TABLE OF CONTENTS

Page

LIST OF FIGURES

1. INTRODUCTION

1.1 Background

Tidal exchange is a major method of transport in and out of coastal bays and inlets. This exchange is critical to many natural processes that maintain a balance between the inlet and the ocean. Many types of fish and animals rely upon the tidal exchange to provide nutrients in and out of the bay. This mixing can pull eggs and small marine animals out into the bay or out into the ocean where they can provide food for larger fish and animals. This process also helps to regulate the chemical composition of the bay so that the animals and vegetation can rely upon a consistent salinity range.

Not only is understanding this exchange vital to understanding the biological processes of tidal inlets, but knowledge of this exchange is necessary to prevent damages due to coastal chemical spills. On March 22, 2014, a collision between the M/V Summer Wind and an oil tank-barge named Kirby 27706 resulted in damage that left approximately 170,000 gallons of oil freely floating in Galveston Bay. This oil was subjected to tidal exchange near the inlet which dispersed it on shorelines from Galveston island to the Matagorda islands. Having this oil stranded across many beaches has caused damage to not only the animals and vegetation located around these beaches but also to property at these locations (Hassan, Anita, et al. "Texas City Dike Closed after Barge and Ship Collide."). By having a more thorough understanding of the tidal transport mechanisms at the inlet to Galveston bay, a more optimized response to the spill may have been realized.

In order to understand the inlet exchange, it is necessary to analyze the mechanisms of tidal transport. When the tide transitions from slack tide to ebb tide, water begins to move through the narrow inlet and forms vortex dipoles on the seaward side. These vortices entrain fluid and particulates that moves through the inlet. Once the vortices reach a particular size they detach from the inlet and, due to their symmetry about the centerline of the inlet, propel each other away from the inlet (Kashiwai (1984), and Whilden (2015)). This method of transport can result in a

high density of chemicals or biological matter being entrained in the vortices and being carried far from the mouth of the inlet.

1.2 Objectives

The research in this thesis is aimed at developing a method for designing a shallow water flume and utilizing the flume to conduct starting jet vortex experiments to validate that the flume is working according to design. The itemized list of objectives for the project are as follows:

- Review the important non-dimensional parameters needed for sizing a shallow water flume capable of conducting starting jet vortex research

- Develop a method for analyzing the parameter space for designing a new shallow water flume

- Conduct and analyze starting jet vortex experiments for known conditions to test the performance of the new flume

2. LITERATURE REVIEW

2.1 Background Work

Early work to analyze the dynamics of shallow vortex dipoles for tidal flow through an inlet was conducted by Wells and Van Heijst (2003); they assumed the behavior of tidal vortices could be described by representing the inlet as a line sink and treating the system as the relationship between a line sink and a dipole. They concluded that $K_w = 0.13$ represents a critical point where the vortices remain in position during a reverse tide, where $K_w = W/UT$; W = inlet width, U = cross-sectionally averaged peak tidal velocity through the inlet and T = tidal period. When $K_w < 0.13$ the vortices propagate out during the reverse tide and when $K_w > 0.13$ the vortices are entrained back into the inlet. This critical value was later tested by Del Roure et al. (2009) in which experiments were conducted that included bottom friction and viscosity. The results of these experiments confirmed that the critical point of $K_w = 0.13$ for potential flows accurately approximates the critical point for flows including friction. [**?**]

With the data collected from the Del Roure et al. (2009) experiments as well as experiments conducted in Whilden (2009), FREHD (Fine Resolution Environmental Hydrodynamics) coarse-grid numerical models were developed and tuned for a one-equation turbulence model in Hutschenreuter et al. (2019). These models were able to accurately predict and track the formation and propagation of the vortex dipoles. These models were able to further confirm the prediction of the critical value of $K_w = 0.13$ for a wide range of hydrodynamic conditions.

2.2 Theory/Governing Equations

The governing equations used for analysis of tidal vortices use the shallow water assumption and the barotropic assumption. The shallow water assumption is safely assumed due to the water depth being much smaller than the inlet width. The behavior of tidal vortices is well encapsulated by the geometric length scales of the inlet width W, the channel length L, and the water depth h, and the kinematic scales of the peak cross-sectionally averaged velocity scale U, and the tidal

period time scale T as was demonstrated in Whilden (2009) and Del Roure et al (2009). These scales can be related by a set of non-dimensional parameters that accurately predict tidal vortex behavior.

The main governing parameter for these experiments is the Inlet Strouhal Number K_W (Wells and Van Heijst, 2003):

$$K_W = \frac{W}{UT} \tag{2.1}$$

The effect of surface waves on the behavior of the tidal vortices is predicted by relating gravity, water depth, and the peak cross-sectionally averaged velocity in the form of the Froude number,

$$Fr = \frac{U}{\sqrt{gh}} \tag{2.2}$$

where g is the gravitational acceleration. When $Fr \leq 0.7$, the effect of stability on the dynamics of the tidal vortices are weak such that their effects are negligible (Ghidaoui et al. (2006)).

In order to quantify the turbulent behavior of the flow, the depth-scale Reynolds number is used.

$$Re_h = \frac{Uh}{\nu} \tag{2.3}$$

where ν is the kinematic viscosity of the fluid. In order to maintain fully turbulent open-channel flow, $Re_h > 1000$ is maintained.

Aside from these non-dimensional parameters, other important characteristic scales that govern the dynamics of the tidal vortices are the tidal excursion length and the frictional length scale.

The tidal excursion length is derived by calculating the maximum distance that can be traveled using a sinusoidal velocity equation (Whilden (2009)).

$$l_t = \frac{Ut}{\pi} \tag{2.4}$$

This equation represents the maximum distance an object in the tidal flow field can travel before it begins to experience a reverse tide.

The frictional length scale demonstrates the distance an object travels before it begins to feel the effects of bottom friction (Signell RP, Geyer WR (1991)).

$$l_f = \frac{h}{c_f} \qquad (2.5)$$

where c_f is the quadratic-law bed friction coefficient. By combining the frictional length scale and tidal excursion length, we are able to create a new non-dimensional parameter that can be used to characterize the bed induced frictional effects felt by a tidal flow field. This parameter is the bed friction effect parameter.

$$B_f = \frac{l_t}{l_f} = c_f \frac{UT}{\pi h} \qquad (2.6)$$

This parameter compares the maximum length the tidal plume will travel with the length needed to feel the full effects of the bottom friction.

3.   FACILITY DESIGN

3.1   Flume Sizing

3.1.1   Facility Review

To begin designing a new facility for conducting shallow water fluid dynamic experiments, a review was conducted of existing facilities for shallow water fluid dynamic experiments. The facility reviewed was the shallow water basin used for previous starting jet vortex experiments (Del Roure et al. (2009), Whilden (2009), Bryant et al. (2012)) located in the Institute for Hydromechanics, Karlsruhe Institute of Technology, Water Research Laboratory.

Figure 3.1 shows the layout of the shallow water basin during the experiments reported in Whilden (2009). The main facility operates through a system of pipes on either side of the flume and a system of butterfly valves that allow for reversible flow. This reversible flow represents a tidal system capable of mimicking the tides in a tidal inlet system. The extensions at the midway point of the flume represent the vertical wall barrier islands used during the experiments.

In order to conduct the starting jet vortex experiments in conditions similar to what would be seen in nature requires that there are minimal effects of the flume boundaries on the vortices. In order to quantify this boundary effect on a propagating vortex, the ratio of the tidal excursion length, l_t, to the width of the basin was analyzed. Empirical data was used from the Del Roure et al. (2009) and Whilden (2009) experiments to determine what l_t to basin width ratios were used in past experiments that gave accurate results. By compiling the data from the experiments in Del Roure et al. (2009) and Whilden (2009) into Figure 3.2, we found that the maximum l_t utilized in the experiments was 6.23 meters.

By using the basin dimensions in Karlsruhe, 5.5m x 15 m, The ratio of l_t to the width was determined to be approximately 1:0.88 and the ratio of l_t to the length was determined to be approximately 1:2.41. Using these ratios allowed for the maximum tidal excursion distance to be selected that could be used without the expectation of significant boundary effects.

6
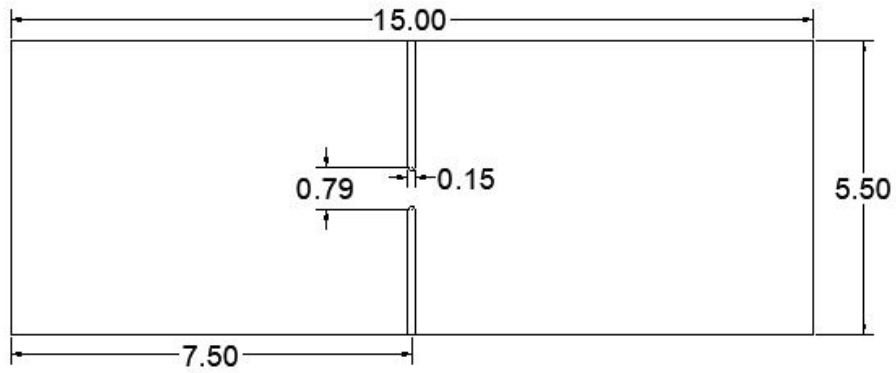
Figure 3.1: Adapted Figure of the Layout of the Experimental Basin Reported in Whilden (2009) (in meters)

Del Roure et al (2009)					
depth (m)	U (m/s)	T (s)	l_t (m)	l_f (m)	l_t/l_f
0.1	0.19	56	3.39	12.80	0.26
0.1	0.19	103	6.23	12.80	0.49
0.1	0.11	41	1.44	11.66	0.12
0.1	0.18	59	3.38	12.70	0.27
0.1	0.16	66	3.36	12.46	0.27
0.1	0.2	53	3.37	12.90	0.26

Whilden (2009)			
depth (m)	l_t (m)	l_f (m)	l_t/l_f
0.09	3.16	12.68	0.25
0.05	3.16	5.88	0.54
0.03	3.16	3.06	1.03

Figure 3.2: Experiment Parameters

Figure 3.3: Location of Buoy g06010

The data in Whilden (2009) showed that with a 3 cm depth there was less coherency to the vortex formation than in the deeper cases. The lack of vortex coherence was assumed to be due to the larger effects of the bottom friction felt by the vortices. By comparing the tidal excursion, l_t to the frictional length scale, l_f, a non-dimensional parameter was developed describing the magnitude of frictional effects expected during one tidal cycle, $B_f = l_t/l_f$. Figure 3.2 shows the values of B_f for each of the experiments in Del Roure (2009) and Whilden (2009). The value of B_f ranges from 0.12 to 1.03 depending on the experiment.

In order to compare the B_f values of the experiments conducted at the shallow water basin located in the Institute for Hydromechanics, Karlsruhe Institute of Technology, Water Research Laboratory to a natural setting, NOAA depth and current data was collected from the Galveston bay entrance. The buoy location is shown in Figure 3.3. By applying the shallow water approximation, the Buoy surface current data in the Galveston Bay Entrance collected in January 2018 was plotted over time in order to establish the U_{max} and U_{min} through the inlet as well as the tidal period during that time, as shown in Figure 3.4. The water depth, h, was determined by averaging depth values from NOAA chart 11324 in the region where the vortex would be forming off of the edge of the jetties. The value of U_{max} is approximately 1.25 m/s, U_{min} is approximately 0.5 m/s, and T is approximately 24 hours. In order to compare the frictional length scale between the field to
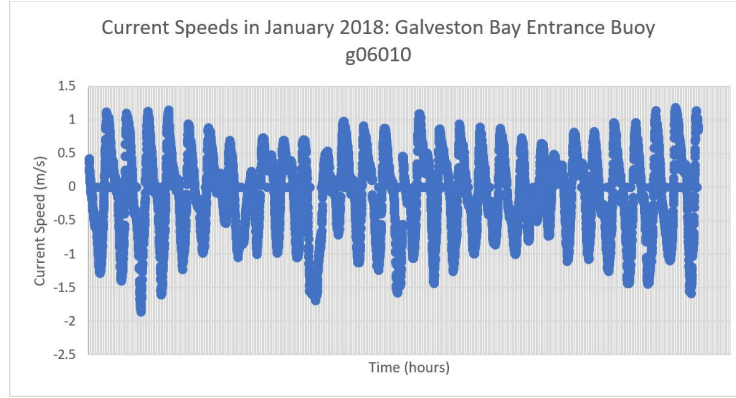
Figure 3.4: Current Data in January 2018

the experimental basin, it is necessary to understand equivalent sand roughness, k_s, for the field conditions. Using the data collected from Figure 3.4, the following characteristic values were calculated over a range of k_s values for the inlet in order to find the sensitivity of each value to the k_s value:

- C_f

- l_f

- l_t

The plots of those values over varying k_s are shown in Figure 3.5. Figure 3.5 shows that for k_s values from 0 m to 0.05 m the C_f value increases by approximately 275%. From k_s values from 0.05 m to 0.15 m, the C_f increases by 75%. This rapid increase at low k_s values is due to the logarithmic relationship between the k_s value and the C_f value that is shown below(Von Carmer (2005), Swamee & Jain (1976)),

$$C_f = \frac{1}{16} * (\log(\frac{k_s/D_h}{3.71} + \frac{5.74}{Re^{0.9}}))^{-2} \tag{3.1}$$

The frictional length scale, l_f, is also heavily driven by k_s at values of k_s less than 0.5. This is because of the inverse relationship between C_f and l_f shown below.

9
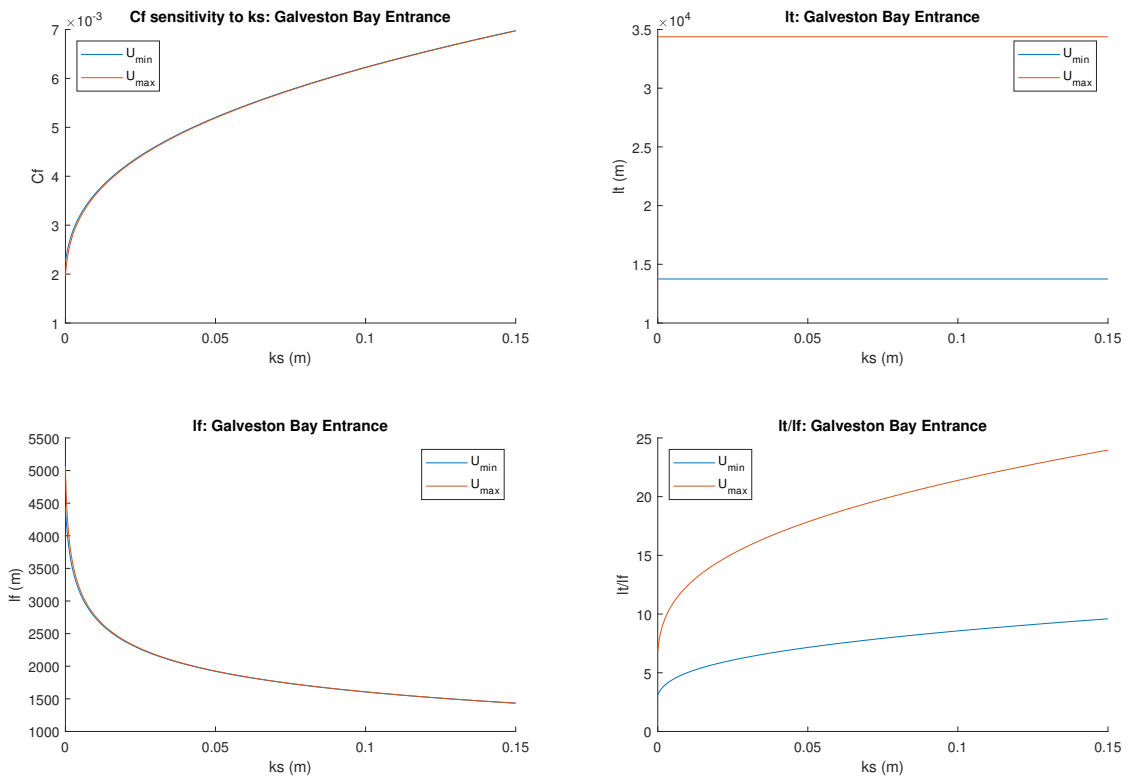
Figure 3.5: Sensitivity to k_s

Galveston Bay Inlet Conditions					
W (m)	T (hr)	h (m)	U (m/s)	K_w	Fr
4000	24	10	0.5 - 1.25	0.04 - 0.09	.05 - .13

Figure 3.6: Representative Values of W, T, h, U, K_w, and Fr for the Galveston Bay inlet in January 2018

$$l_f = \frac{h}{C_f} \qquad (3.2)$$

Figure 3.5 also shows that the range of B_f varies from roughly 4 to 25 depending on the U and k_s values. In order to further elucidate the role that the previous ratio plays in the life cycle and behavior of the initial starting dipole, it was necessary to compare the value obtained by the previous field analysis to relevant laboratory work conducted in Del Roure et al. (2009) and Whilden (2009). Figure 3.2 shows that in previous work the B_f value was generally below 1 which means that the friction plays a minimal role in the behavior of the dipole; whereas, in the field the scale ratio is of the order O(10) so that friction plays a much larger role in the behavior of the dynamics. Taking this difference into account, the facility was designed to be capable of generating experiments with higher l_t/l_f values than were utilized in the Del Roure et al. (2009) and Whilden (2009) experiments. Values of W, T, h, U, and a range of K_w and Fr for the Galveston Bay inlet in January of 2018 are shown in Figure 3.6.

3.1.2 Parameter Space

In order to generate experiments capable or representing realistic flow conditions, a parameter space capable of recreating these conditions was developed. The flowchart in Figure 3.7 describes the process used to determine the parameter space for choosing experiments.The steps used to obtain the full parameter space are as follows:

1. Set the Fr and Re_h limits for the flume and choose the initial basin dimensions and K_w value to find the parameter space for

2. Choose the range of water depths to solve for

3. Solve for the U_{min} and U_{max} in the flume

4. Find maximum l_t for chosen basin dimensions

5. Solve for maximum inlet width, W, in the flume

6. Find the range of possible T

7. Solve for remaining parameters $l_f, B_f, Re_h, and Fr$

For step 1, the initial limiting parameters chosen were:

- $Re_h \geq 1000$

- $Fr < 1/3$

- $K_w = [.11, .13, .15]$

- $Dimensions = 8ft$ x $16ft$

In step 2, the water depths chosen were to allow for similar W/h ratios as were utilized in Whilden (2009) and Del Roure et al. (2009). After initially setting the parameters and choosing the water depth in steps 2 and 3, Re_h and Fr are both solved for U in step 4 by using the following equations:

$$U_{max} = Fr\sqrt{gh} \tag{3.3}$$

$$U_{min} = \frac{\nu Re_h}{h} \tag{3.4}$$

By setting the value for Fr and Re_h equal to the chosen limiting values from step 1, U_{min} and U_{max} can be solved for and plotted over a range of water depths. By following this procedure, a plot similar to what is shown in Figure 3.8 is obtained.

Set K_w, Re_h min, Fr max, and Basin Dimensions: B x L

Set range of Water Depths

Solve for maximum allowable l_t using basin dimensions

$$l_{t2} = \frac{B}{0.88}$$

$$l_{t1} = \frac{L}{2.41}$$

$$l_t = \min(l_{t1}, l_{t2})$$

Solve for range of U using Fr and Re_h limits

$$U_{min} = \frac{1000\nu}{h}$$

$$U_{max} = \frac{1}{3}\sqrt{gh}$$

Find max W from l_t and K_w equations

$$UT = \pi l_t$$

$$W = K_w UT$$

Find range of T from K_w equation

$$T = \frac{W}{K_w U}$$

With U, T, h, and W, solve for l_f, B_f, Re_h and Fr
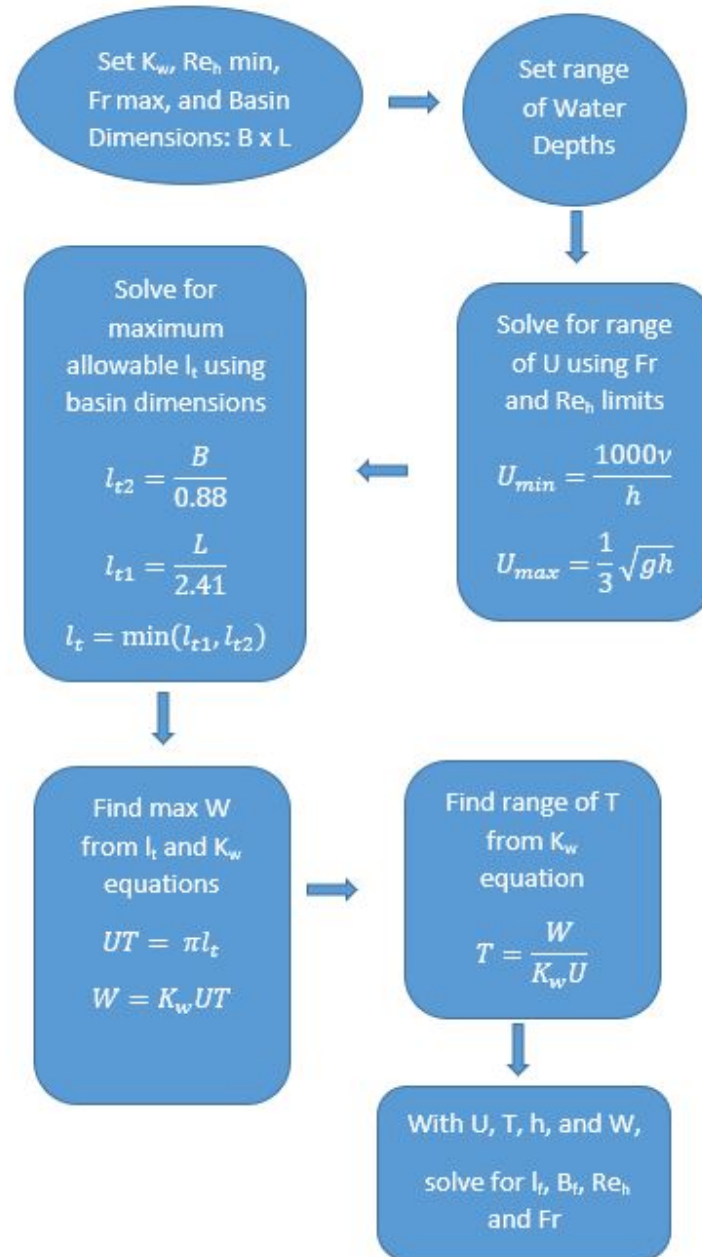
Figure 3.7: Parameter Space Methodology
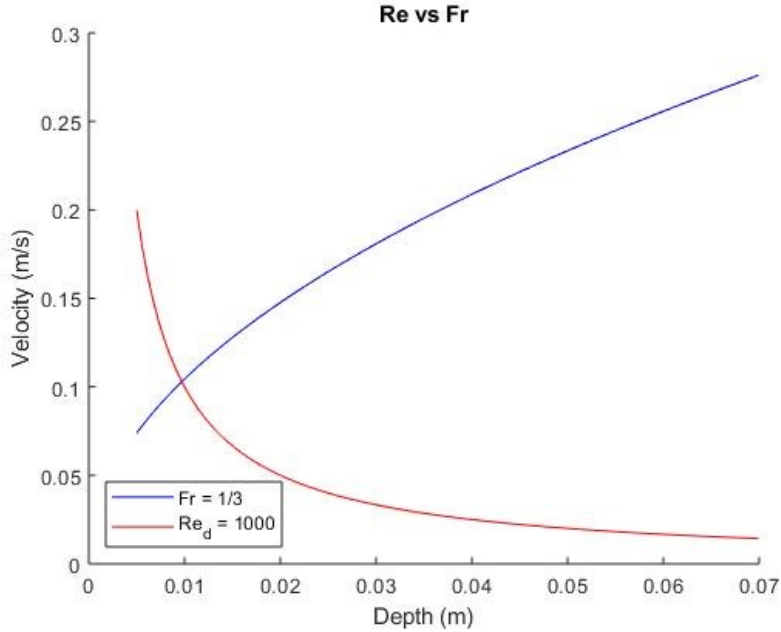
Figure 3.8: Re_h vs Fr

Figure 3.8 allows the acceptable range of velocities to be visualized. By staying below the blue and above the red lines, we are able to stay within the chosen Re_h and Fr limits that we set for the calculation.

In step 4, we assume a maximum allowable tidal excursion length to basin length scale, L, of 1:2.41 and a maximum allowable tidal excursion length to basin width, B, scale of 1:0.88. By comparing the two values of tidal excursion length correlating to each of these basin length and width ratios and choosing the smaller value, we are able to determine the maximum allowable tidal excursion length, l_t, for the initial basin dimensions.

From this ratio, in step 5, we can find the maximum allowable inlet width in the flume. To do this, we find the maximum allowable UT from $l_t = UT/\pi$. We then plug this UT into the K_w equation to find the maximum W for a given K_w as is shown in equation 3.5.

$$W_{max} = K_w UT \tag{3.5}$$

Where W_{max} is the maximum width of the inlet.

14
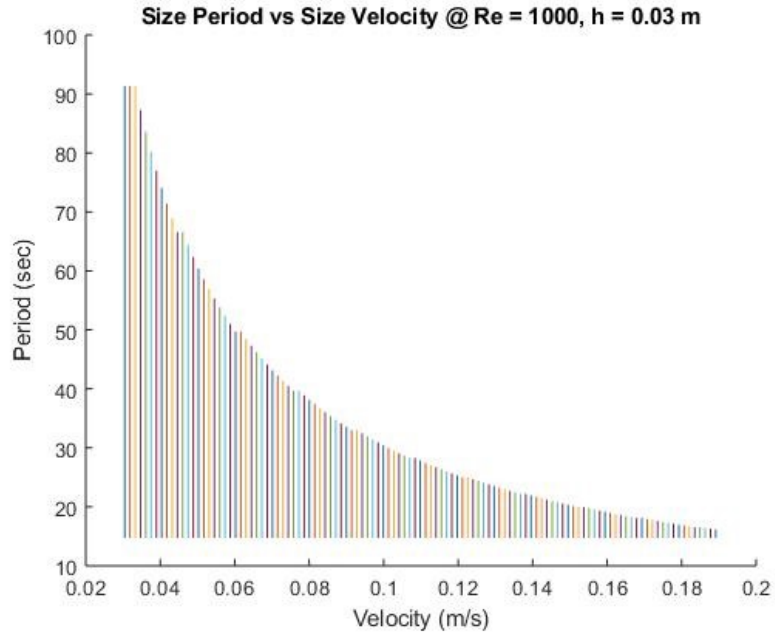
Figure 3.9: Range of T

This width can then be used in step 6 along with the range of acceptable velocities and the chosen K_w in order to apply equation 3.6 to solve for the range of acceptable periods. A plot of the range of periods is shown in Figure 3.9.

$$T = \frac{W_{max}}{K_w U} \tag{3.6}$$

By using the range of U, T, h, W_{max}, and the initial flume dimensions, we were then able to calculate the range of possible values of Fr, B_f, l_f, and Re_h for the chosen K_w condition in the flume. An example of the parameter space developed with an initial $K_w = 0.11$, $B = 5$m, $L = 10$m, is shown in Figure 3.10.
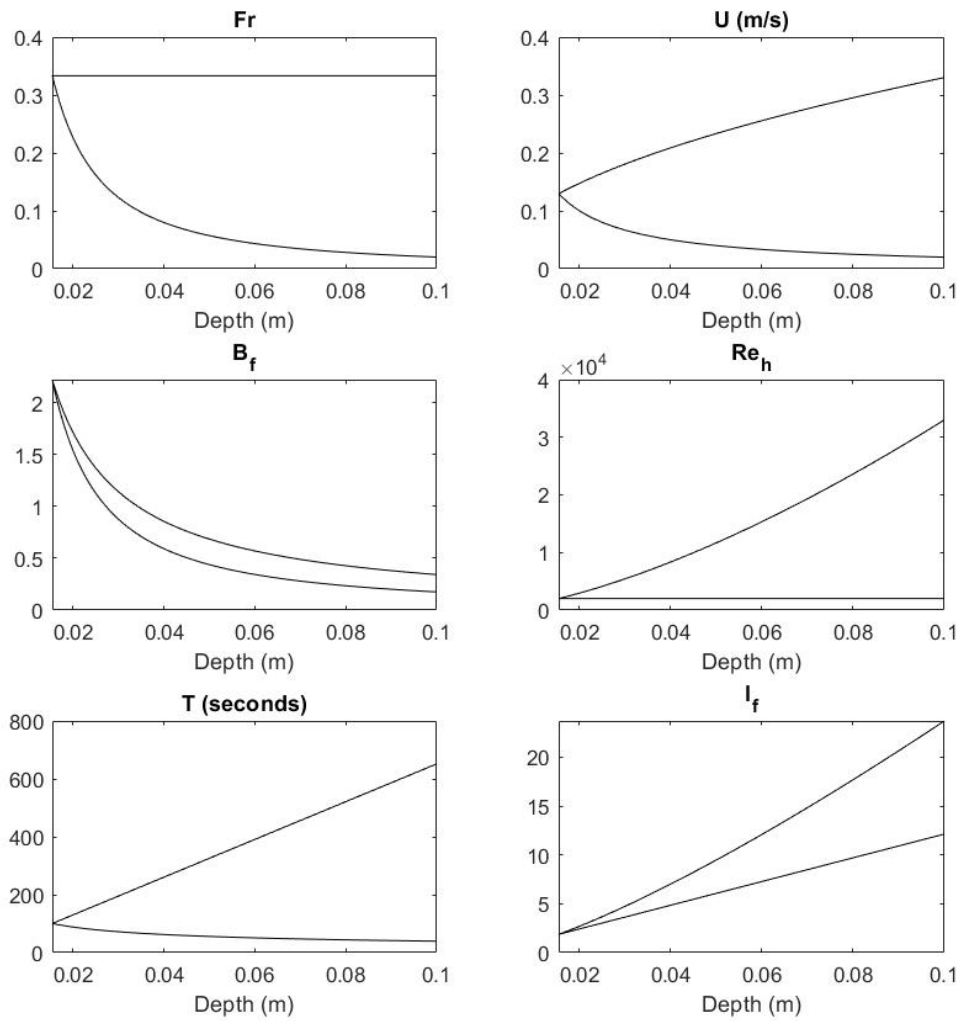
Figure 3.10: Parameters Space for Flume with $B * L = 5$ m $*10$ m at $K_w = 0.11$

3.1.3 Standing Wave Resonance Analysis

In order to avoid standing wave resonance in the tank, the period of seiching was calculated, T_s, in the tank for various lengths and modes for each of the three water depths. To perform this analysis, the Merian Formula was utilized (Dean and Dalrymple (1995)),

$$T_s = \frac{2l}{n\sqrt{gh}} \tag{3.7}$$

This equation is derived by applying the shallow water assumption to the linear dispersion relation such that the phase speed, $C = \sqrt{gh}$, and the wavelength, $L = 2l/n$, where l is the maximum width of the basin and n is the number of oscillations of the waves within the basin.

Figure 3.11 shows the period for seiching modes 1 through 4 for different basin lengths. By making the assumption that the flume is a shallow basin with linear waves and by choosing a period larger than the plotted line values in each of the three plots, generating any wave resonance in the flume due to seiching can be avoided.
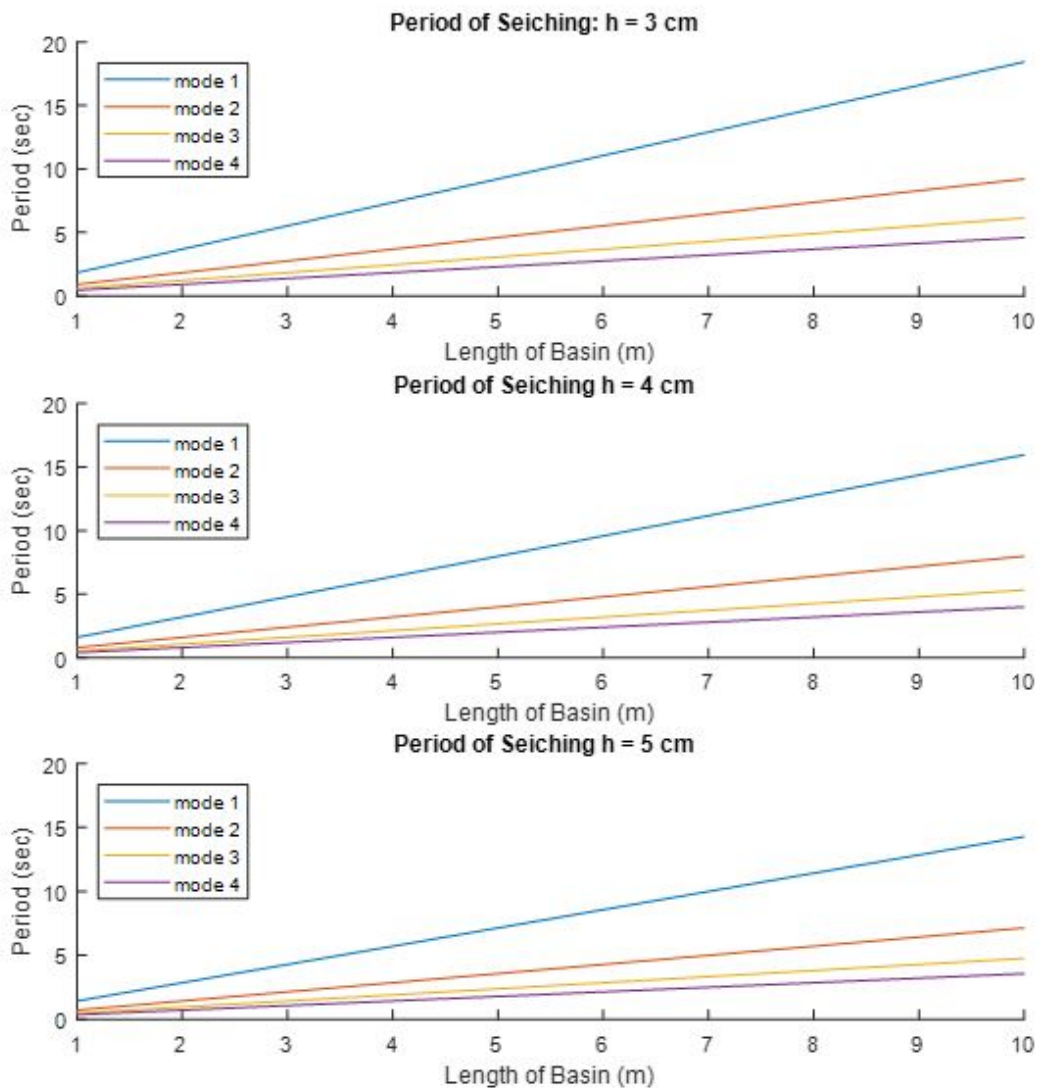
Figure 3.11: Period of Seiching for Different Depths

3.1.4 Flume Dimensions

After developing the methodology needed to select a dynamically similar parameter space, several different flume dimensions were considered. The flume sizes were chosen for their ready availability to be constructed from standard cuts of tempered glass and from the space limitations in the Environmental Fluid Dynamics Laboratory on the Texas A&M University System Rellis Campus, these sizes were:

- 4ft x 4ft

- 4ft x 8ft

- 4ft x 16ft

- 8ft x 8ft

- 8ft x 16ft

In order to determine the limits imposed on the chosen experimental parameter space due to each of the different layouts, an analysis of l_t was conducted. By using the ratio of l_t to the width of approximately 1:0.88, and the ratio of l_t to the length of approximately 1:2.41, the maximum l_t of each layout can be established. By analyzing the data shown in Figure 3.12, it can be seen that the largest l_t value can be achieved in the 8ft x 16ft basin by almost a factor of 2 from the second highest l_t value. This is important to the design of the facility because having a larger l_t value brings the ratio of B_f closer to what would be observed in a field setting such as was demonstrated for the Galveston bay inlet.

In order to visualize the best case parameter space for each of the layouts with maximum B_f, the Fr, l_f, B_f, U, T, and Re_h were plotted for each layout with $K_w = 0.11$ over a series of different water depths. These plots are shown in Figures 3.13 - 3.17.

By comparing the B_f values for each of the layouts shown in Figures 3.13 - 3.17, the advantage of using the 8ft x 16ft size can be quantified. The 8ft x 16ft layout is the only case where all of the B_f values up to a depth of 3cm can be over 1. This means that experiments conducted in this setup

19

B(ft)	L(ft)	l_t max (m)
4	4	0.51
4	8	1.01
4	16	1.39
8	8	1.01
8	16	2.02

Figure 3.12: Maximum Tidal Excursion due to Layout Dimensions
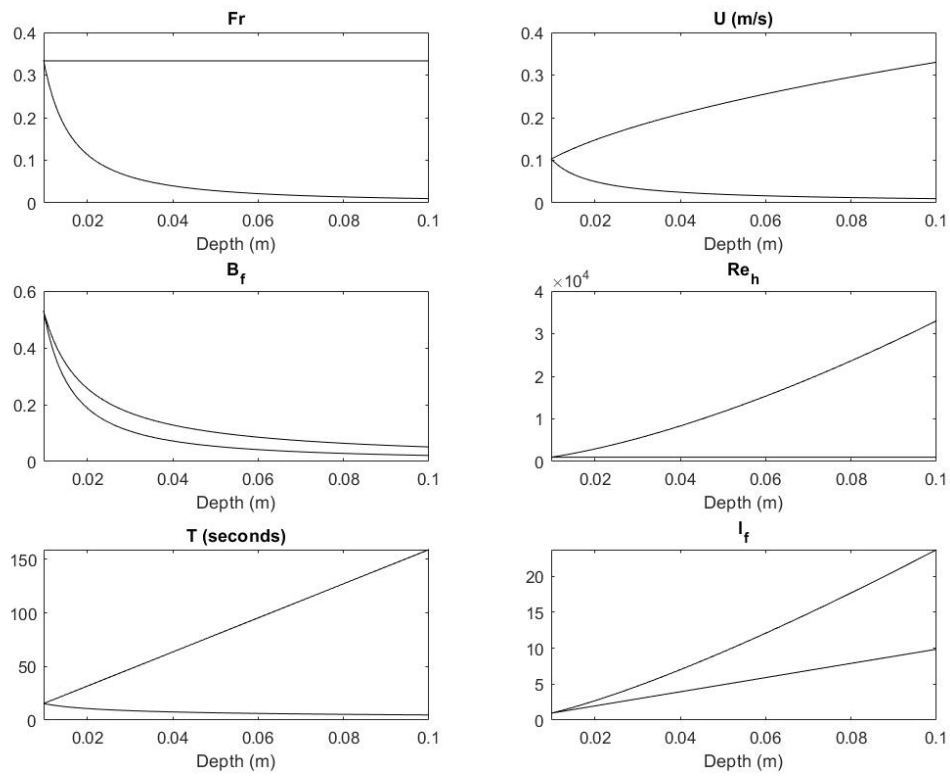
Figure 3.13: 4ft x 4ft Layout Parameter Space at $K_w = 0.11$
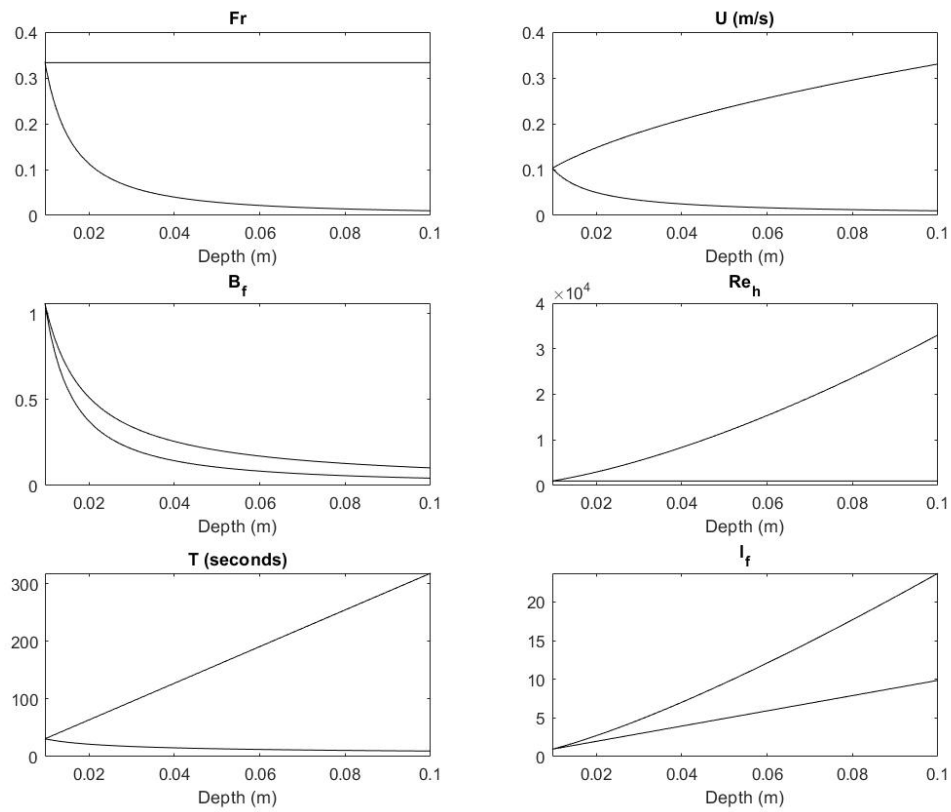
Figure 3.14: 4ft x 8ft Layout Parameter Space at $K_w = 0.11$
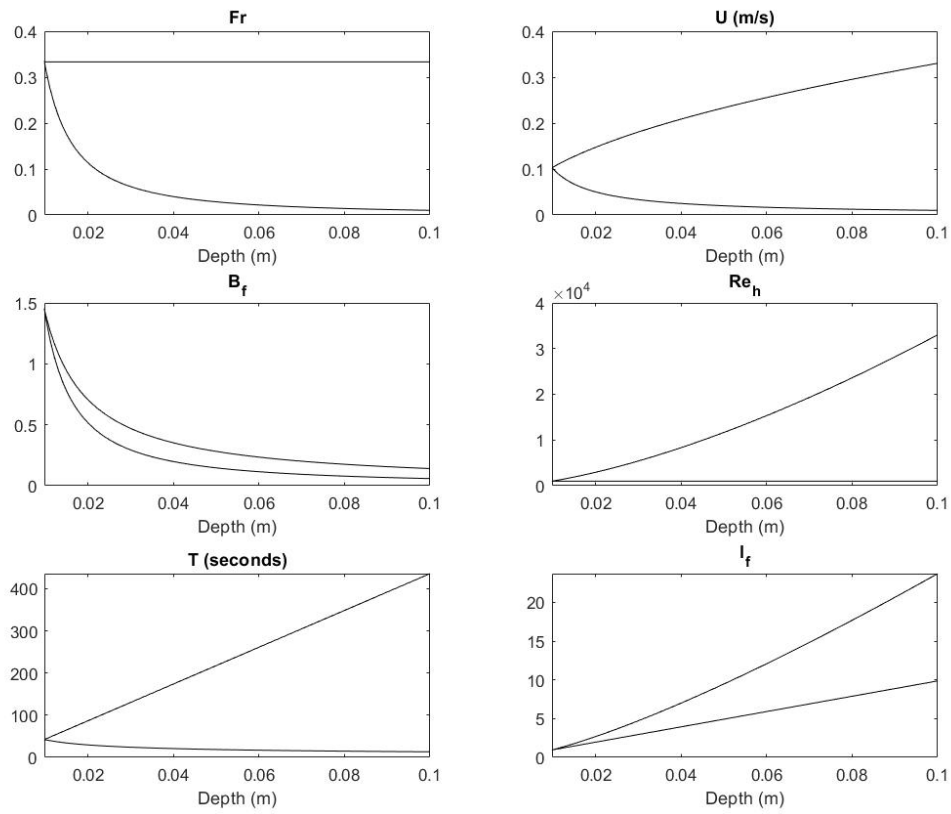
Figure 3.15: 4ft x 16ft Layout Parameter Space at $K_w = 0.11$
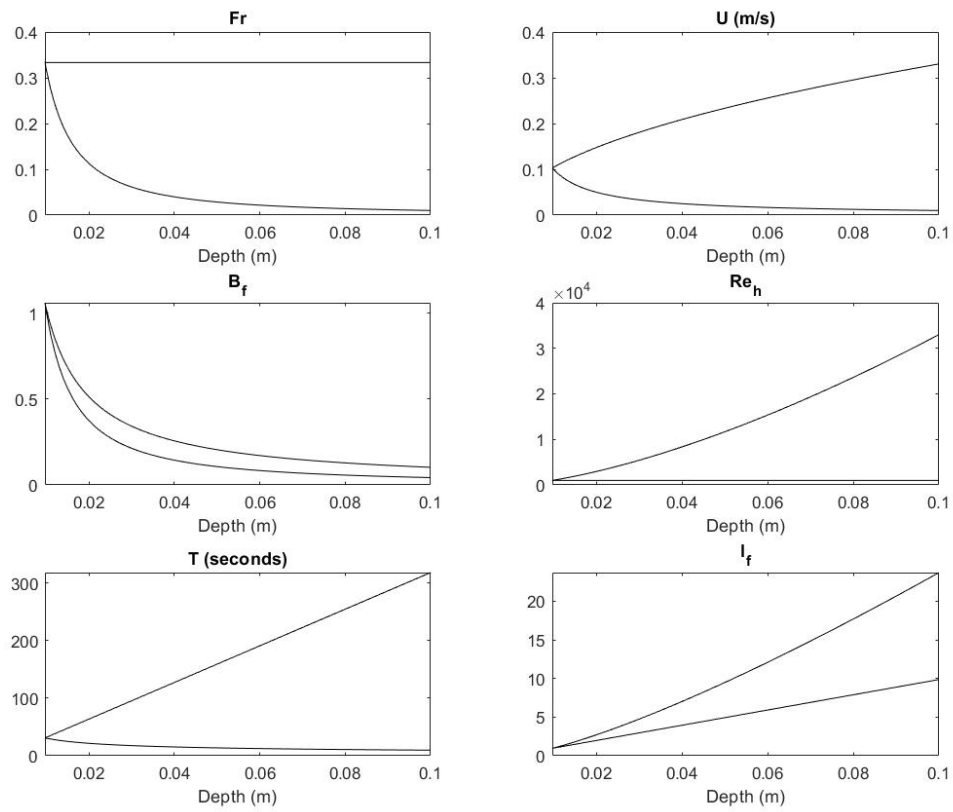
Figure 3.16: 8ft x 8ft Layout Parameter Space at $K_w = 0.11$
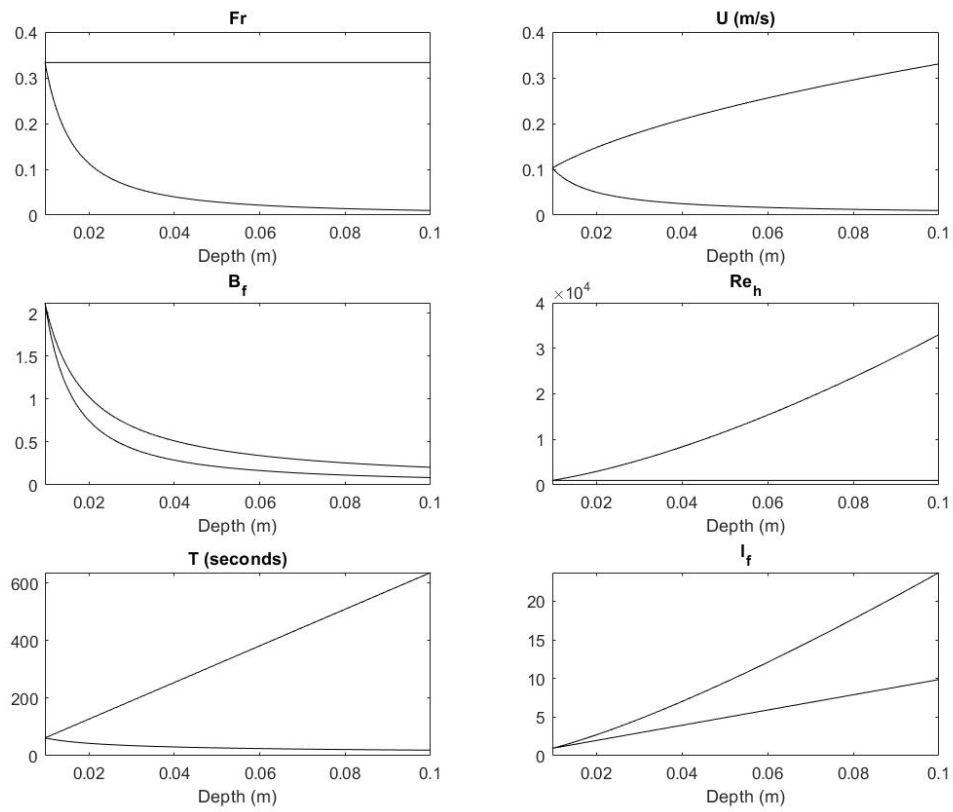
Figure 3.17: 8ft x 16ft Layout Parameter Space at $K_w = 0.11$

are most closely aligned with what would be expected in a field test. Since the 8ft x 16ft layout allows for the highest range of B_f values of all the different layouts, this is the layout that was selected for the design. This design also respects the criteria Re_h 1000 and $Fr < 0.7$; likewise, the desired range of K_w can be achieved without causing basin wave resonance.

3.2 Structural Design

3.2.1 Deflection Analysis

3.2.1.1 Beam Deflection

Due to the limited space in the Environmental Fluid Dynamics Laboratory on the Texas A&M University System Rellis Campus, the shallow water flume was designed to be raised above the ground so that the pipe system and electrical equipment could be comfortably situated below the flume. In order to maintain enough space for the equipment, the glass bottom for the flume was designed to be located at a height of 4 feet off of the ground. To determine the size of components needed to prevent glass breaking, deflection analysis was conducted for the beam deflection holding the glass bottom in the new shallow water flume.

In order to determine the size of beam needed, it was first necessary to determine the load that would be seen on each beam. By assuming an initial spacing of 16 inches between each beam and a maximum water depth of 6 inches, the force of water with a density of 62.4 lb/ft^3 felt by each beam is approximately 20.832 lb/in. Since tempered glass has an approximate density of 0.1 lb/in^3, and by assuming constant contact with the beam, the load from the $\frac{3}{4}$ inch thick glass on each beam is approximately 7.2 lb/in. To allow for people to safely stand on the flume for experimental setup, these loads on the beam were converted to point loads for the most conservative loading estimate. By multiplying the load by the length of the 8 ft beam, the maximum point load felt on each of the horizontal beams is approximately 450 lb.

The material used for the beam calculations was chosen to be aluminum square tube due to the flat surface and aluminum's resistance to oxidization. This provides an advantage to steel which would increase the weight of the frame and would undergo oxidization without proper coating. Since the yield strength of the chosen aluminum 6063 is approximately 31 ksi and the maximum designed point load for the system is approximately 450 lb, failure of the beam due to shear is not possible under normal operating conditions.

To calculate the maximum deflection of the beam supporting the glass and water along the 8 ft
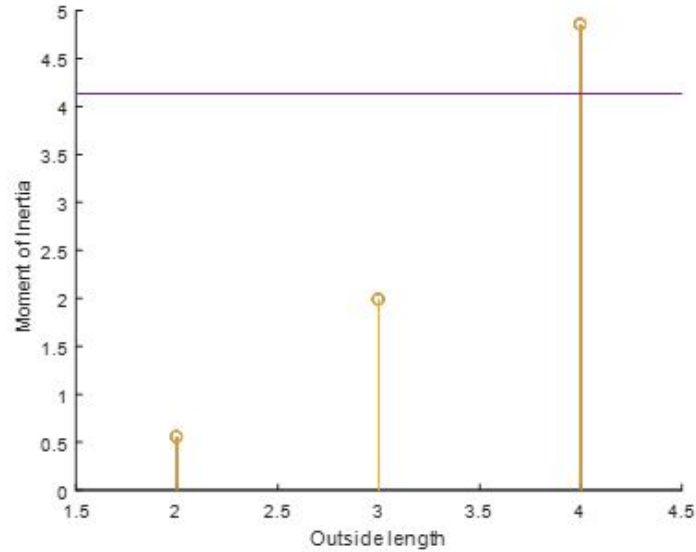
Figure 3.18: Moment of Inertia for 2in, 3in, and 4in Aluminum Square Tube

width of the flume, the beam was treated as a simply supported, center loaded beam. By choosing a maximum deflection of 5 mm in the beam, the size of the beam needed was calculated with the following deflection equation where the length of the beam, L, is 96 inches and the young's modulus for aluminum 6063, E, is 10,000 ksi:

$$\delta = \frac{PL^3}{48EI} \tag{3.8}$$

$$I = \frac{PL^3}{48E\delta} \tag{3.9}$$

where P is the point load, L is the length of the beam, and I in the moment of inertia. Since I takes the following form for a squared tube,

$$I = \frac{h_o^4 - h_i^4}{12} \tag{3.10}$$

the minimum outside side length of the Aluminum square tube beam needed was calculated. The plot of the minimum I needed, along with three standard sizes for Aluminum square tube beams with 1/4 inch thickness are shown in Figure 3.18.

27
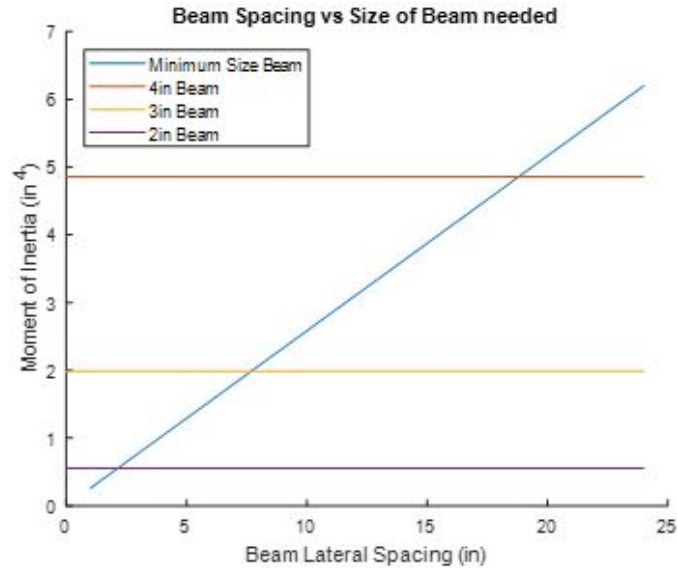
Figure 3.19: Beam Spacing vs. Size of Beam Needed

By choosing an aluminum square tube beam of 4 inch outside by 3.75 inch inside side lengths, the maximum deflection in the beam will be limited to less than 5 mm at maximum loading. In order to see the minimum size beam needed to keep deflection below 5 mm for different spacings, Figure 3.19 was generated by solving the deflection equation for a changing tributary force area. Based on Figure 3.19, a beam of 4 inch square tube aluminum with a spacing of 16 inches was sufficient to limit the beam deflection to an acceptable level.

3.2.1.2 *Glass Deflection*

By using the ASTM standard practice for determining load resistance of glass in buildings (ASTM E1300 (2016)), the maximum deflection and the deflection that will actually occur due to the loading for our specific experiments can be determined for the $\frac{3}{4}$ inch tempered glass. Under the assumptions in the guidelines, the design standards are applied to wind loads, snow loads and self loads up to 210 psf, but since the loads applied to the glass will be much less than 210 psf it can be assumed that this analysis will provide an accurate estimate for the glass deflections.

By selecting fully-tempered, $\frac{3}{4}$ inch thick, 4 ft x 8 ft, and simply supported on four sides glass, the non-factored load (NFL) was analyzed using Figure A1.11 in the ASTM E1300-16 manual.

Since the assumed plate length and width are 2438.4 mm and 1219.2 mm respectively, Figure A1.11 shows that the NFL = 10 kPa = 209 psf. We can then utilize Table 1 in the ASTM E1300-16 manual to determine the glass type factors for the glass. By assuming a long duration loading of water on the glass and using FT for fully tempered glass, the selected GTF becomes 3.0. With the GTF and NFL the load resistance, LR, can be determined by using the following equation:

$$LR = NFL * GTF = 209 * 3.0 = 627 psf \tag{3.11}$$

With an LR of 627 psf and an area of the glass of 32 ft^2 the $Load * Area^2$ is equivalent to 627 psf $*(4$ ft $*8$ ft $)^2 = 642048$ lbft $^2 = 642.048$ kip*ft ^{2}. By using the $Load * Area^2$ and the aspect ratio of 2, Figure A1.11 in the ASTM E1300-16 manual shows that the maximum deflection allowable is approximately 20 mm. Since the maximum loading for the shallow water flume will be approximately 75 psf, the maximum deflection for a single 4ft x 8ft sheet of $\frac{3}{4}$ under the maximum loading condition would be less than 5 mm. A loading of 75 psf is well within the maximum load resistance and since the maximum deflection of the beams was calculated to be less than 5 mm and there are beam supports every 16 inches, the glass will not break under maximum loading conditions.

3.2.2   Assembled Frame

With the beam sizing and spacing finalized, the frame for holding the glass flume was designed and generated in SOLIDWORKS. The frame was designed to be supported by sixteen 4 foot legs made of 4 inch square tube aluminum held in place by 3 inch square aluminum tube. The legs of the flume were designed with adjustable caster wheels to allow for the water level in the flume to be leveled out before experimentation. A truss was created on either end out of 2 inch aluminum tube to resist horizontal forcing. This initial design is shown in Figure 3.23.

After the initial frame was designed, two tanks made out of 3/16 inch steel sheets were designed for either end of the flume. The tanks were designed a 4 inch diameter hole placed in the same side to allow for the pipe system to output into and suction out of either side of the flume.
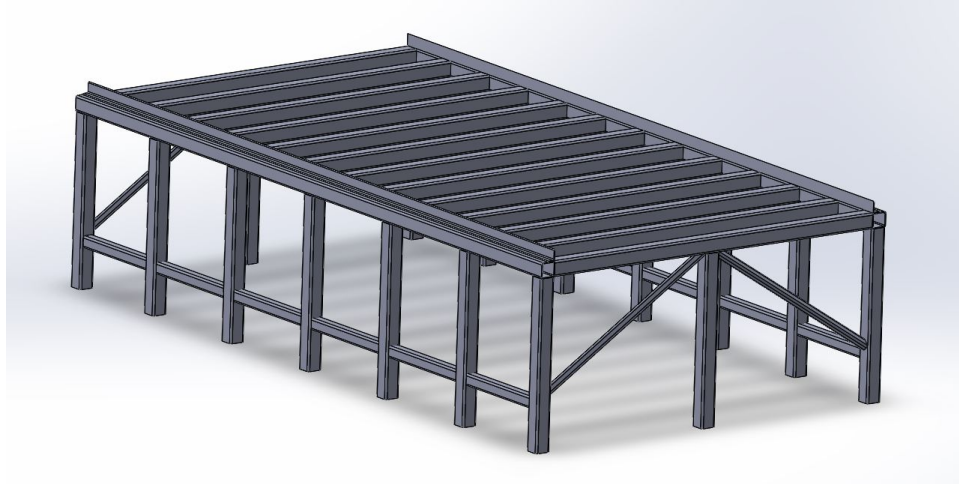
Figure 3.20: CAD Drawing of Aluminum Frame for Glass
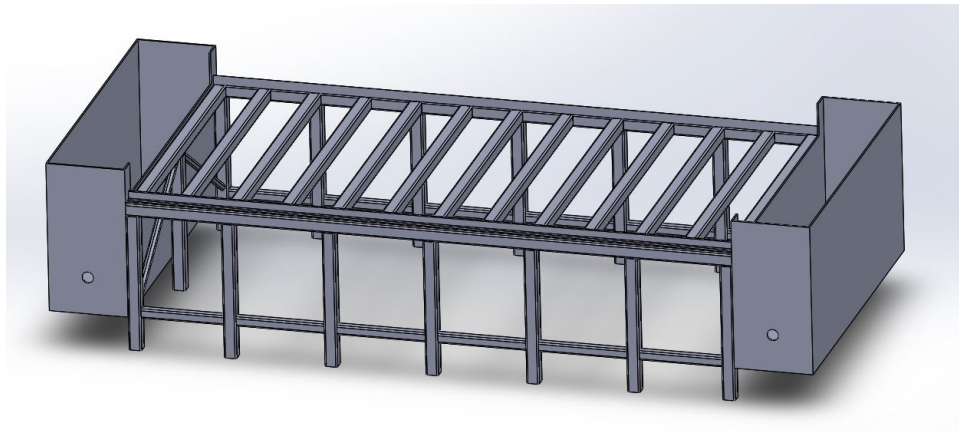
Figure 3.21: CAD Drawing of Aluminum Frame for Glass with Side Tanks

This input and output is the driving mechanism for the flow across the flume in either direction. A CAD drawing of the flume with the tanks on either side is shown in Figure 3.24.

In order to get the flume to fit into the Environmental Fluid Dynamics Laboratory on the Texas A&M University System Rellis Campus, the flume was initially built in two sections cut lengthwise down the middle of the flume. Half inch steel plate was welded onto the cut ends of the beams to allow the plates on either side of the cut to be bolted together on site. To add stability to the frame due to the frame being modularly assembled, two 4 foot legs were added near the center of the

flume. Once the two halves of the frame were assembled, the tanks were attached to the frame at either end.

Figure 3.22: Schematic of Pipe System

Electronic Components			
	Model	Manufacturer	Model Number
Pump	2 HP Straight Centrifugal Pump	Dayton	2ZXN7
Flow Meter	3 inch Electromagnetic Flow Meter	FLOMEC	465C66
Variable Frequency Drive	VLT Micro Drive	Danfoss	DAN132F0012

Figure 3.23: Electronic Components

3.2.3 Pipe System

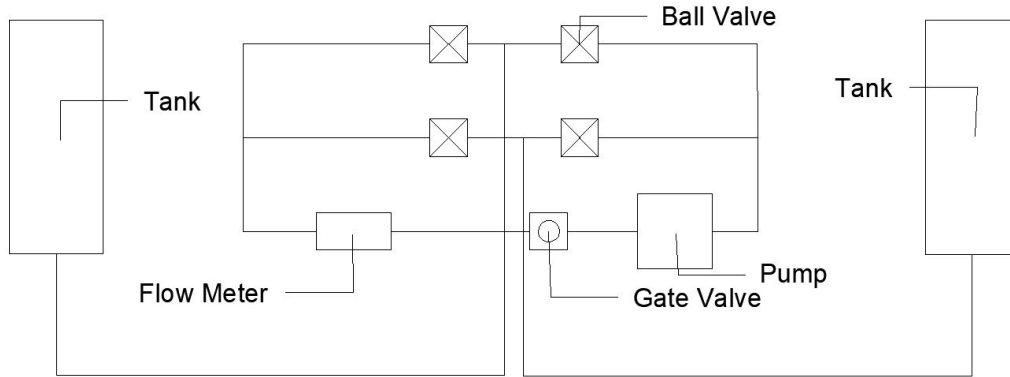In order to pump water between the tanks, a pipe system was designed for the flume as shown in Figure 3.25. This system is made up of a pump, a gate valve to throttle the flow, an electromagnetic flow meter to record real-time flow rate data, and a system of ball valves to allow for reversible flow. The flow reversal works by opening and closing opposite pairs of valves such that the output of the pump switches which tank it flows into. The specific electronic components used in the system are listed in Figure 3.26.

To uniformly distribute the flow into each tank, a line diffuser made of 2 inch PVC pipe extending 8 feet lengthwise along each tank was installed as is shown in Figure 3.27. The pipe has holes along each side designed such that the sum of the area of the holes, A_n, and the area of the pipe cross-section, A_{pipe}, have the following relationship $\sum A_n = A_{pipe}$ to maintain an even pressure at each hole in the pipe. This flow from the pipe then travels through a 2 inch thick layer

Figure 3.24: Line Diffuser

of rubberized hair with a plastic backing, before it reaches a flow straightener made of 0.5 inch x 8.5 inch straws to aid in flow uniformity across the flume.

To control the pump, a custom signal is generated using NI SignalExpress and is sent via a NI Data Acquisition Board to the variable frequency drive. The frequency drive then controls the frequency and voltage of the signal sent to the pump in order to generate the desired flow pattern. To record the actual flow pattern generated by the pump, the flow meter can be connected via RS-485 to USB interface to a computer in the lab for data collection.

4. METHODOLOGY

4.1 Set of Experiments

To determine the set of experiments needed to be conducted, an analysis of the parameter space capable of being produced by the new facility was conducted. To define the parameter space, several parameters were evaluated for different values of W, U, T, and h. The parameters evaluated are as follows:

- Re_h

- Fr

- Kw

- l_t

- l_t/l_f

- W_i/W

The first parameter that was analyzed was the barrier island width to the inlet width, W_i/W. In order to maintain geometric scaling between the experiments conducted in Del Roure et al. (2009), and Whilden (2009), the W_i/W was used as a scaling factor. A schematic of these values in relation to the basin layout is shown in Figure 4.1.

Figure 4.2 shows that for Whilden (2009) the ratio of W_i/W is 0.19 while in Del Roure et al. (2009), the ratio of W_i/W is 0.13. In order to keep the current experiments geometrically similar, these values were used to determine possible barrier island configurations for the experiments. The range of values that fit these ratios is shown in Figure 4.2. In this figure, the blue lines that intersect the possible value circles show the 3 standard aluminum square tube sizes that could be used. The 4 inch barrier island width was selected due to the reduction of l_t that would result from using the smaller 2 inch width, and the potential boundary effects that could occur by making the inlet
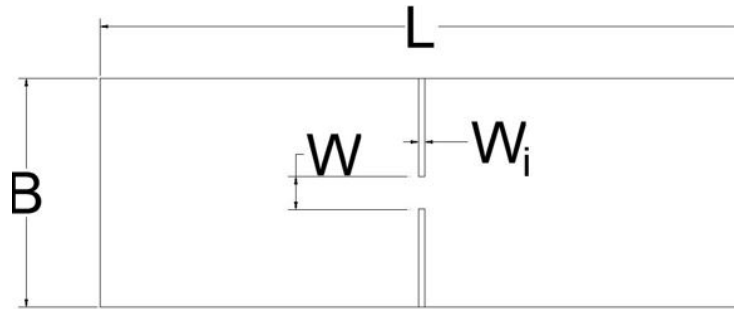
Figure 4.1: Schematic of Basin Layout

(in meters)	Whilden (2009)	Del Roure et al(2009)
W_i	0.15	0.15
W	0.79	1.17
W_i/W	0.19	0.13

Figure 4.2: W_i/W Comparison (Whilden, 2009), (Del Roure et al, 2009)

width > $1/3$ of the total flume width, by using the 6 inch case, which was never conducted with past experiments in Del Roure et al.(2009), Whilden (2009), and Bryant et al.(2012). By using $W = 20.75$ inches based on the W_i value selected in Figure 4.3 and by setting $K_w = 0.11$, Figure 4.4 was generated showing the value of the other governing parameters at the new geometrically similar inlet. Figure 4.4 shows that the limits of the parameters of $Fr < 0.7$, and $Re_h \geq 1000$ are satisfied for 2 cm water depth and above. In order to maintain the largest B_f values and still have varied depths in the experiments, the experimental set that was chosen is shown in Figure 4.5.
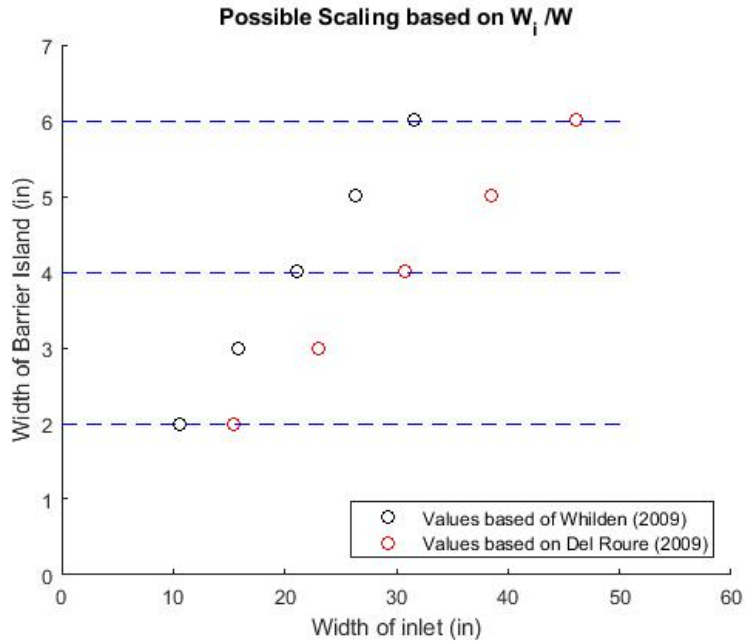
Figure 4.3: W_i/W Scaled Values (Whilden, 2009), (Del Roure et al, 2009)

4.2   Experimental Setup

To track the formation and propagation of the tidally generated starting jet vortices, surface PIV was conducted. The main pieces of equipment that were used for the experiments are the following:

- Phantom Miro M340

- FLOMEC Electromagnetic Flow Meter

- Danfoss Variable Frequency Drive

- 2 HP Dayton Centrifugal Pump

- NI Data Acquisition Board

- Wave Frequency Generator

- Polypropylene Particles

36
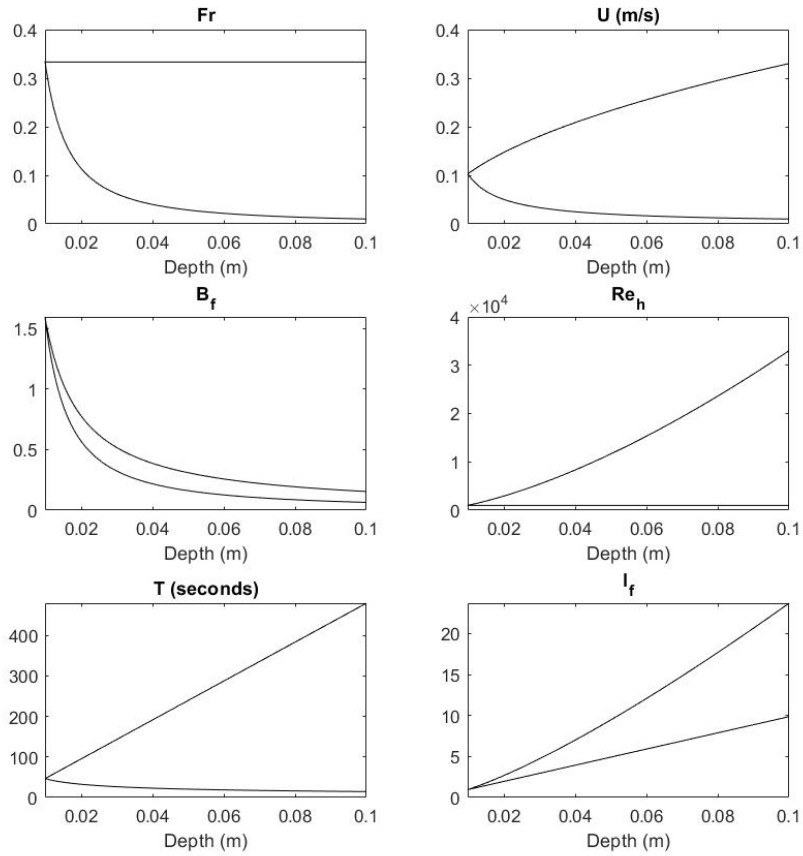
Figure 4.4: W_i/W Scaled Parameter Space with $W = 0.527$ m and $K_w = 0.11$

Depth (cm)	U (m/s)	T (s)	Kw
2	0.02	66	0.35
2	0.04	66	0.20
2	0.08	98	0.07
3	0.07	66	0.11
3	0.06	66	0.13
3	0.08	66	0.10
5	0.05	66	0.17
5	0.05	66	0.15
5	0.07	98	0.07

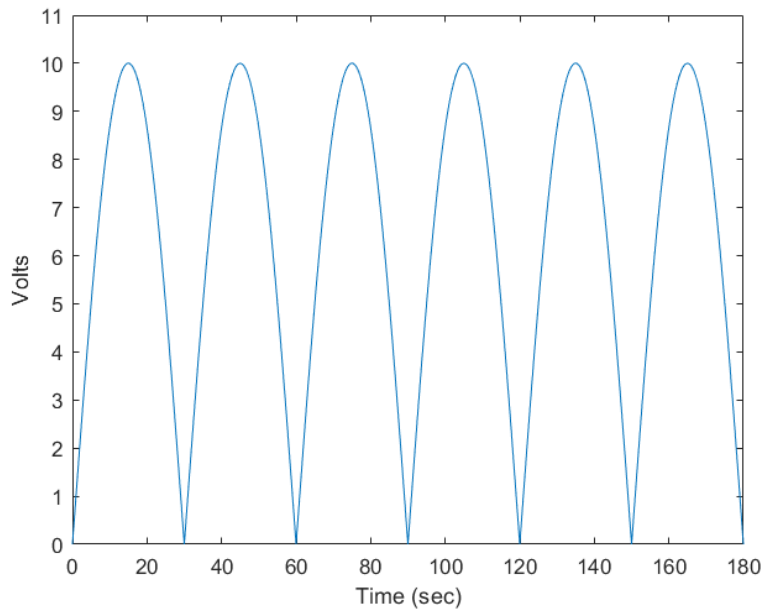Figure 4.5: Experimental Parameter Space

Figure 4.6: Signal Pattern

- HDX 1000-Watt Halogen flood lights

In order to generate the tidal flow, a sinusoidal signal was generated using NI Signal Express and sent to the variable frequency drive via the NI Data Acquisition board. The variable frequency drive then adjusts the voltage and frequency to the pump following the sinusoidal pattern. This varied voltage causes the rpm of the pump to ramp up and ramp down in a manner representative of a sinusoidal tidal flow. An example of the signal sent is shown in Figure 4.6.

The flume operates as a closed system, in which a configuration of four ball valves is used to reverse the flow at slack tide conditions. Real-time measurements of the flow rate are taken every 0.1 sec by the flow meter and are sent via RS-485 serial connection to a computer where the signal is analyzed and plotted.

In order to take images of the positively buoyant polypropylene particles, the Phantom Miro M340 high speed camera was mounted above the flume and is angled down on one side of the inlet in order to capture the flow dynamics. The water in the flume is seeded with polypropylene particles so that the captured images could be correlated using surface PIV to track the particle
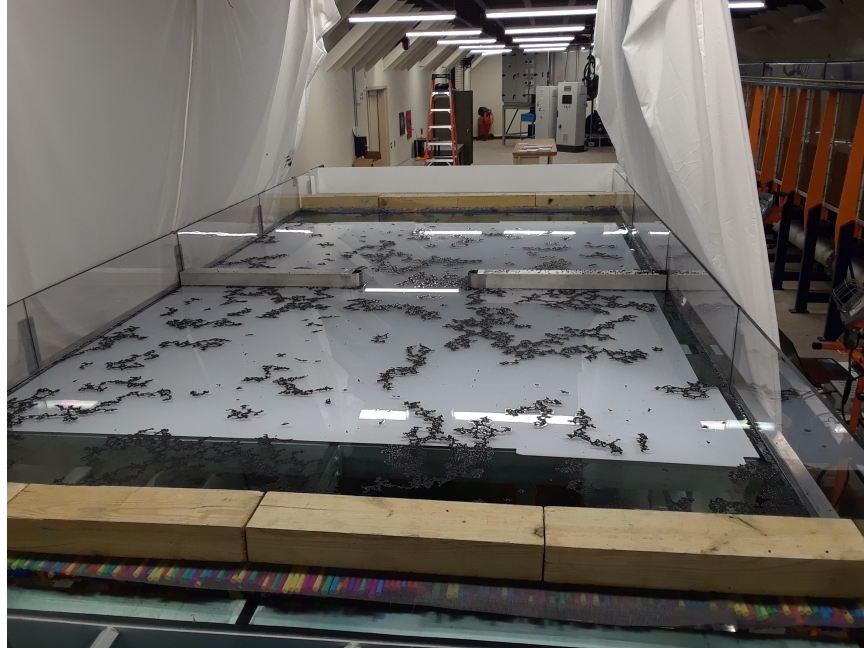
Figure 4.7: Flume Setup for Experiments

motions. The Phantom Miro 340 was externally triggered by a wave signal generator to provide manual control of the frames per second captured during experimentation. To maintain uniform lighting in the flume, the flume was surrounded with 4 1000-Watt Halogen flood lights with cotton sheets hanging between the flood lights and the flume to create diffuse lighting. This setup is shown in Figure 4.7.

4.3 Flow Validation

4.3.1 Flow Validation

4.3.1.1 Pump Performance

In order to determine the accuracy of the pump performance with the input signal from the variable frequency drive, an analysis was conducted on the data recorded by the flow meter. The flow meter data was collected every 0.1 s via RS-485 interface and recorded on a computer. An example of this data is shown in Figure 4.8. This data shows a step-like slope because the flow meter has a maximum refresh speed of approximately 0.4 seconds. To determine the fit of the
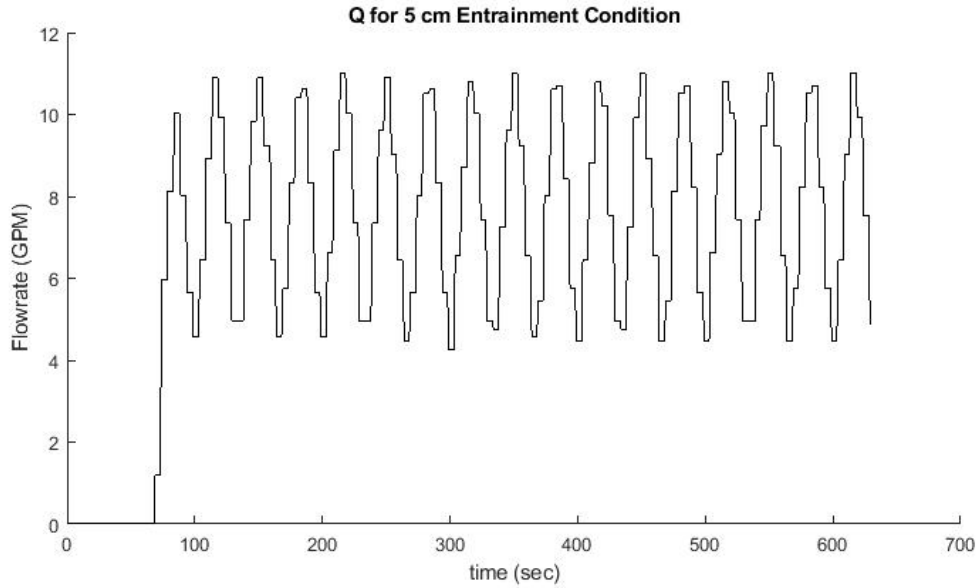
Figure 4.8: Raw Data 5 cm Entrained Condition

recorded points with a regression line, each incremental point of identical value was removed so that only the point where the value changes in each data log is plotted. This data is then fit to a sinusoidal function.

$$y = a_1 abs\big(\sin(a_2 t + a_3)\big) + a_4 \tag{4.1}$$

where a_1 is the amplitude, a_2 is the frequency, t is the time, a_3 is the phase shift, and a_4 is the y displacement.

The data points and the regression line were then plotted together to compare the fit of the data to the expected signal behavior, as is shown in Figure 4.9. The plot for the 5 cm $K_w = 0.15$ case shows that the pump is outputting a flow regime consistent with the custom tidal flow signal sent via the variable frequency drive.
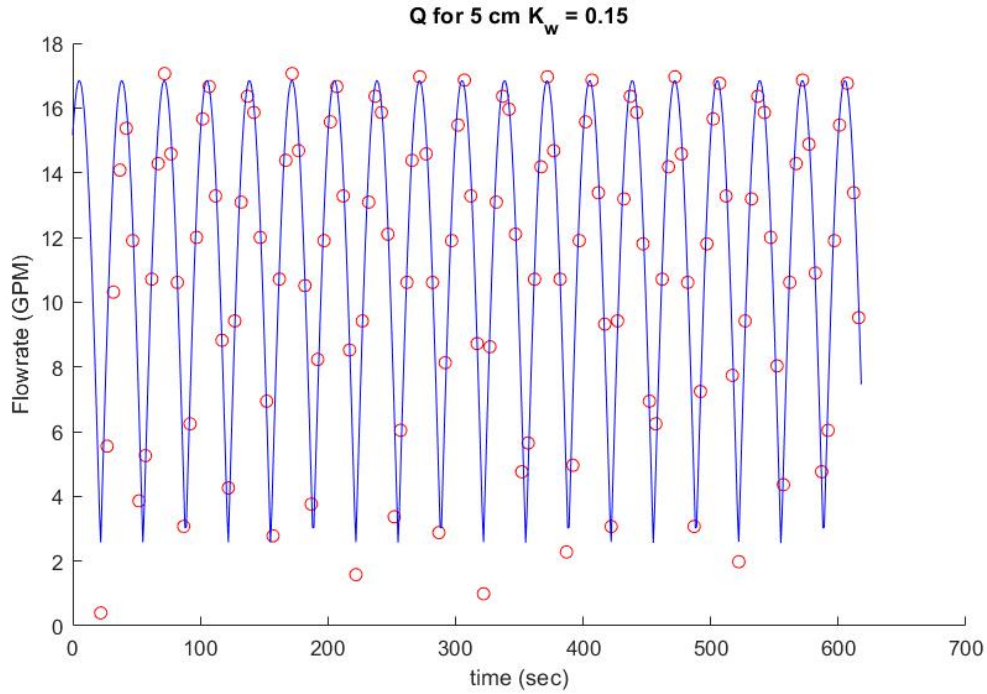
Figure 4.9: Comparison of Data Points to Regression Line 5 cm $K_w = 0.15$ Case

4.3.1.2 Uniformity

To determine the uniformity of the flow field, dye visualization was conducted for a steady state flow condition at 3 cm. A schematic showing the coordinate system and the direction of flow is shown in Figure 4.10. Figure 4.11 shows that in the positive x-direction there was a slight bulge in the velocity field, so further surface PIV analysis was done to quantify the irregularity in the flow field. Figure 4.12 shows approximately uniform flow across the flume. By looking at Figure 4.13, the flow irregularity can be seen in red while the mean flow is in blue. To further elucidate the deviation from the mean, Figure 4.14 shows the percent error from the mean at each point along the width of the flume.
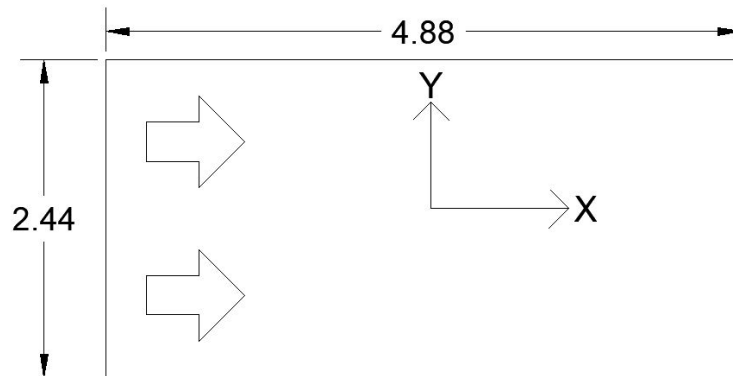
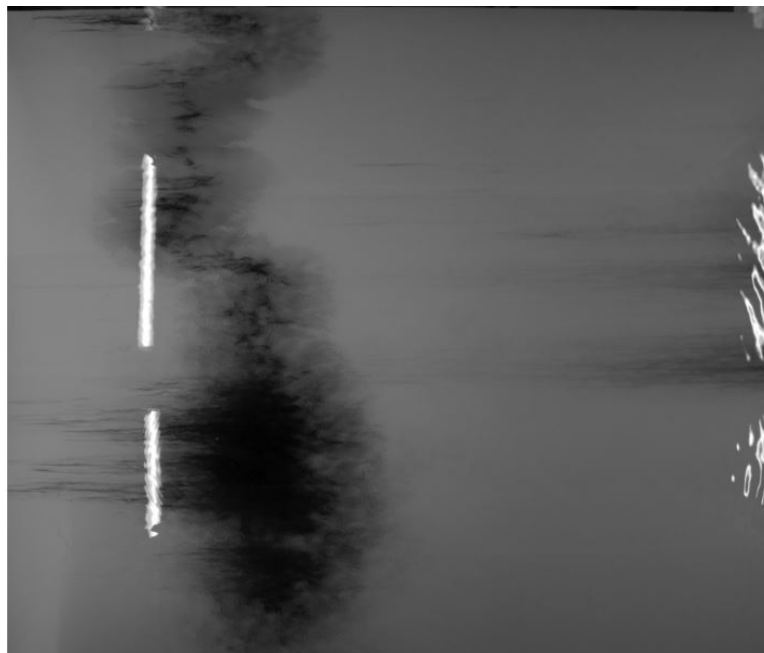Figure 4.10: Layout of Flume with Flow Moving in Positive x-direction (Units in Meters)

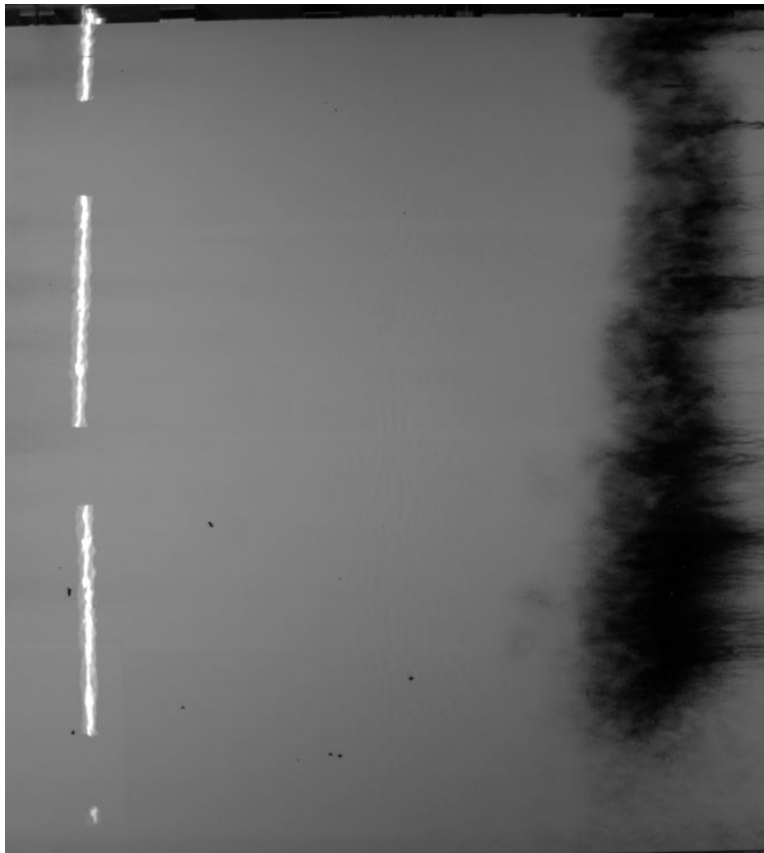Figure 4.11: Dye Visualization in Positive x-direction

Figure 4.12: Dye Visualization in Negative x-direction
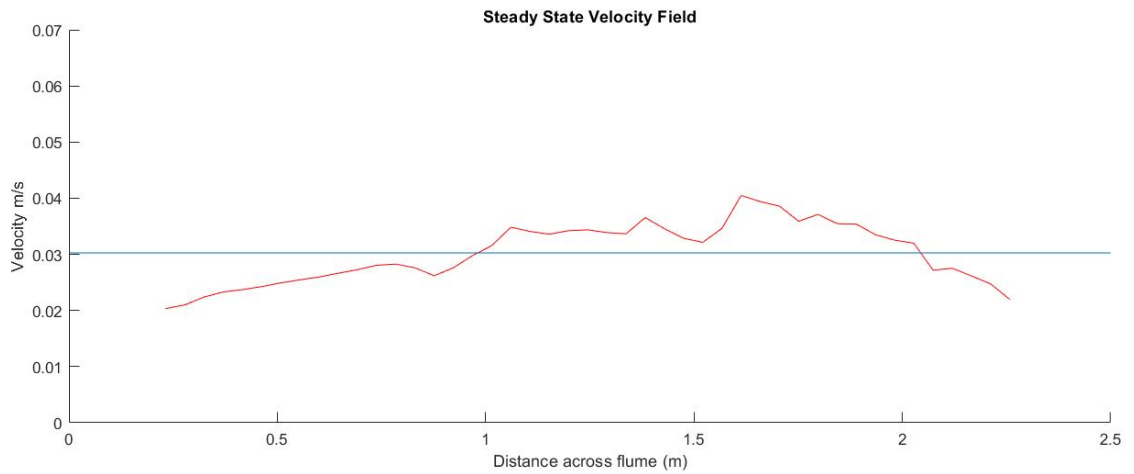

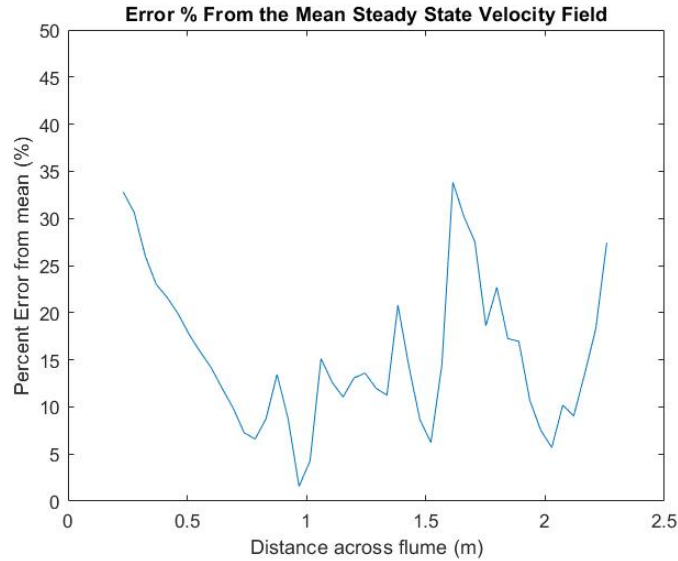Figure 4.13: Steady State Velocity Field in Positive x-direction

Figure 4.14: Error % From the Mean Steady State Velocity Field. Flow in Positive x-direction

4.4 Surface PIV Analysis

In order to determine the correct range of particles sizes that can be utilized by the camera with differing lenses and differing focal lengths, Figure 4.15 was generated. The minimum and maximum particle sizes were chosen to be 1.5x - 5x the pixel size as was utilized in Weitbrecht, V., G. Kuhn, and G. H. Jirka (2002). They also determined that the best particle material to use for surface PIV is polypropylene. Based on the ranges found above, the standard 3 mm polypropylene pellet size created for industry fit the necessary conditions. We sourced our particles from Independent Plastic, Inc.

4.4.1 Preprocessing

To analyze the raw images taken during the experiment, the particle image velocimetry software PIVlab (Thielicke, W. and Stamhuis, E.J. (2014)) was used. The raw images were uploaded to the software and a mask was drawn to cover the inlet. This mask set all of the vectors values within the drawn mask to NaN so that they would not be considered in the velocity calculations. After the mask was applied to the image, contrast limited adaptive histogram equalization (CLAHE), introduced in Pizer et al. (1987), was applied to the images to increase the contrast between the particles

44

14 mm Lens					
Distance (ft)	Pixel Size (mm)	Range of Particles Diameter (mm)		FOV (m)	
		Min	Max	Length	Width
6	1.306	1.959	6.53	3.34336	2.0896
5	1.089	1.6335	5.445	2.78784	1.7424
4	0.871	1.3065	4.355	2.22976	1.3936

24 mm Lens					
Distance (ft)	Pixel Size (mm)	Range of Particles Diameter (mm)		FOV (m)	
		Min	Max	Length	Width
6	0.762	1.143	3.81	1.95	1.219
5	0.635	0.9525	3.175	1.625	1.016
4	0.508	0.762	2.54	1.3	0.812

35 mm Lens					
Distance (ft)	Pixel Size (mm)	Range of Particles Diameter (mm)		FOV (m)	
		Min	Max	Length	Width
6	0.523	0.7845	2.615	1.33888	0.8368
5	0.435	0.6525	2.175	1.1136	0.696
4	0.348	0.522	1.74	0.89088	0.5568

Figure 4.15: Particle Sizing

and the background. Instead of optimizing the whole image in a single histogram, CLAHE breaks the image into smaller tiles that can have their individual histograms optimized to increase image contrast. After optimizing the individual tiles, bilinear interpolation is conducted between each tile to get a smooth transition between each individual tile, thus increasing the probability of valid vector detection by up to $4.7 \pm 3.2\%$ (Shavit et al. (2007)).

4.4.2 PIV Analysis Method

The PIV analysis was conducted using a discrete Fourier transfrom (DFT) multi-pass algorithm (Thielicke, W. (2014)). The algorithm was conducted on the images using a three-pass process with a 50% overlap between interrogation windows. The interrogation window size for the first pass, second pass, and third pass were 128x128 pixels, 64x64 pixels, 32x32 pixels respectively. According to Keane & Adrian (1990), the maximum displacement between windows should by less than $1/4$ of the interrogation window size. For the images analyzed, this value was approximately
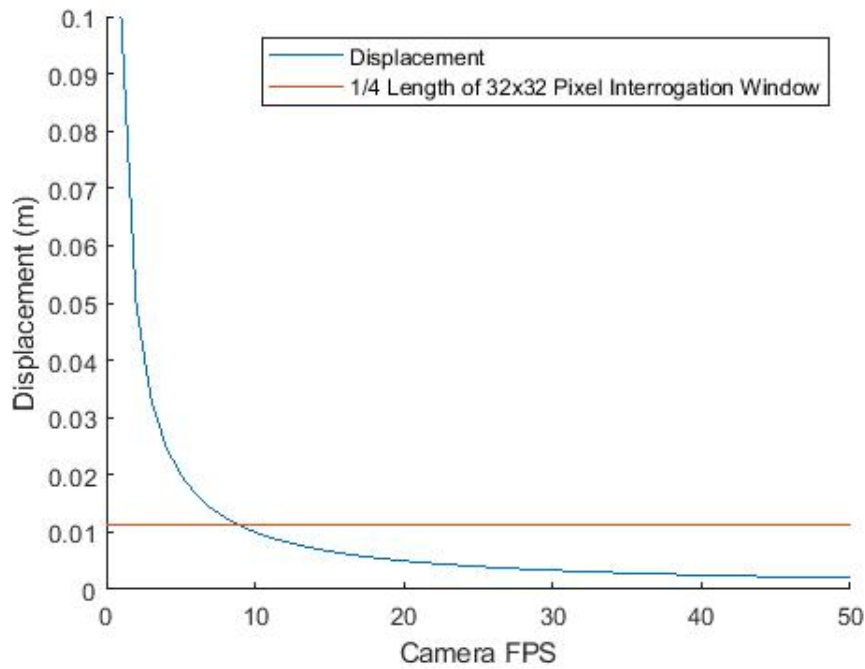
Figure 4.16: Displacement of Particles in Relation to Camera Frame Rate

44.8 mm such that the maximum displacement needed to be below 11.2 mm. To determine the frame rate for the camera needed to keep displacements below 1/4 of the 32x32 pixel window, the displacement vs. frames-per-second (fps) plot was generated in Figure 4.16. This figure shows that the intersection occurs at approximately 9 fps. In order to ensure that the displacement will not fluctuate over 11.2 mm, 12 fps was chosen for the experiments.

4.4.3 Calibration and Vector Validation

The images were calibrated by using a known distance in the image and applying that calibration distance to all displacements in the images. Since we know that the width of the barrier island is 4 inches, we can use that distance to calibrate all of the displacements in the image. Along with the distance, the time step is calibrated by converting 12 fps to 83.333 ms between each image. The calibration image is shown in Figure 4.17.

The vector interpolation was conducted by using a boundary value solver. Stamhuis & Videler (1995) tested the boundary value solver among several popular methods for data interpolation
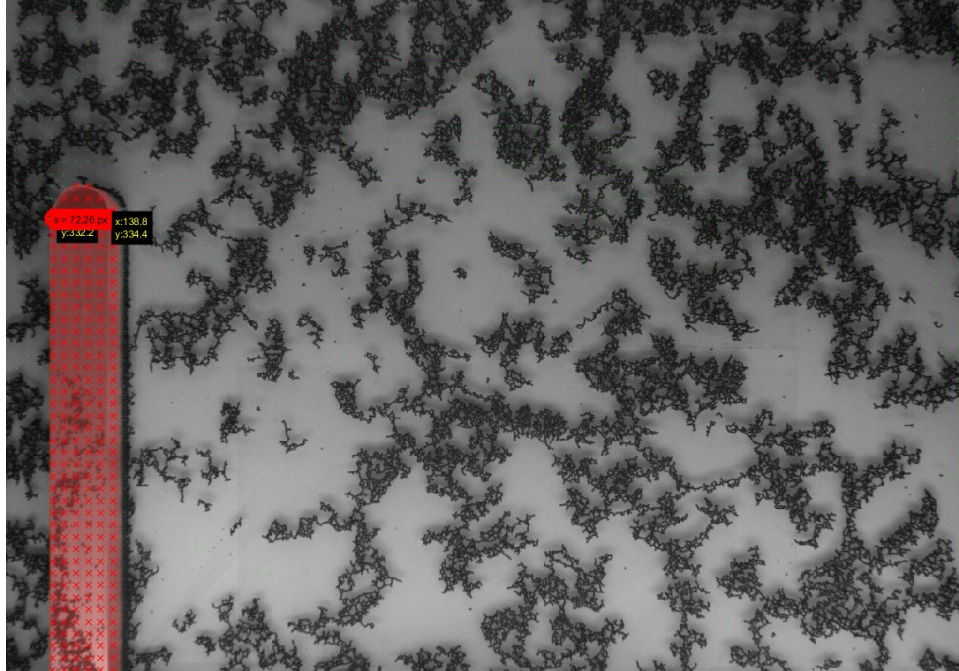
Figure 4.17: Calibration Image

such as the 3x3 mean, 2D linear, 2D piecewise curvic hermite, and 2D spline and found that the boundary value solver performed the best with $> 10\%$ missing data. Since the vector field for the surface PIV has many areas with no vectors, it was utilized to provide the most accurate results. A standard deviation filter was also applied that eliminated vectors that were 7 times the standard deviation. Finally a local median filter (Westerweel & Scarano (2005)) was applied to the vectors with a threshold of 5. This median filter applies the filter to 3x3 regions of vectors in order to locally eliminate outliers without affecting the entire flow field.

Figure 4.18 shows a sample set of images taken from one of the conducted experiments. Figure 4.19 shows the vector map generated by performing the previous analysis to the set of images. Green vectors indicate vectors created from particle motion and orange vectors indicate interpolation.
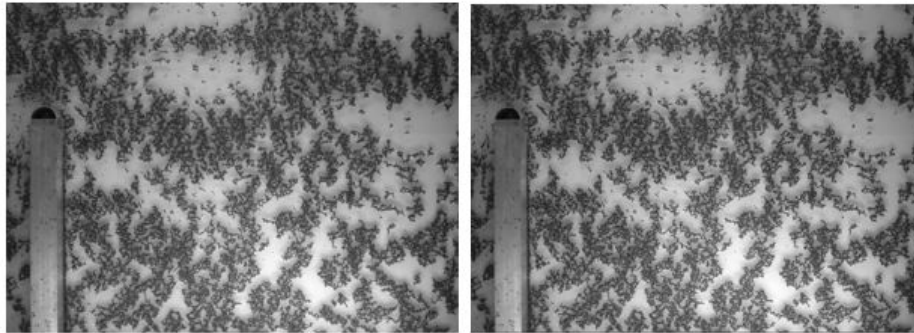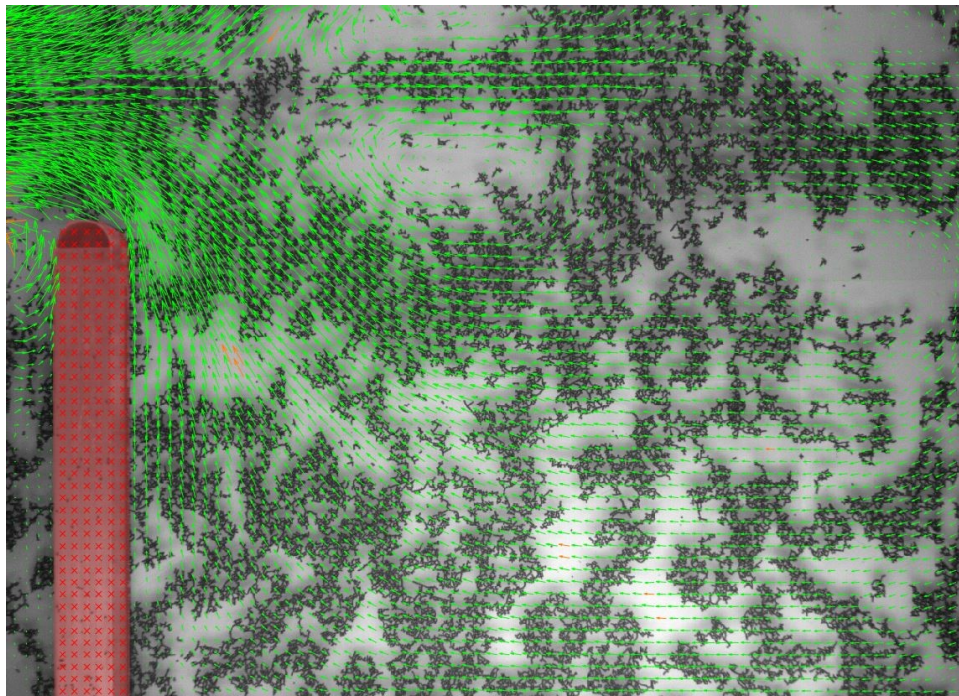
Figure 4.18: Sample Image Pair

Figure 4.19: Vector Map from Sample Image Pair in Figure 4.18

4.4.4 Vortex Detection

After determining the velocity vector fields for an image sequence during an experiment, a method is applied to detect and track the main vortex. To detect the vortex, the swirl strength of the flow field is calculated via the method in Adrian & Christiansen (2000). In this method the following 2D deformation tensor is solved for the flow field,

$$D^{2D} = \begin{bmatrix} \frac{du}{dx} & \frac{du}{dy} \\ \frac{dv}{dx} & \frac{dv}{dy} \end{bmatrix} \tag{4.2}$$

$$\lambda = \left(\frac{du}{dx} + \frac{dv}{dy} \right)^2 - 4\left[\left(\frac{du}{dx}\frac{dv}{dy} \right) - \left(\frac{du}{dy}\frac{dv}{dx} \right) \right] \tag{4.3}$$

The discriminate of the complex eigenvalue of Equation 4.2 is then solved for using Equation 4.3. The discriminate d is solved across the vector field and then, following the method of Stamhuis Videler (1994), is converted to a non-dimensional parameter where 255 indicates a strong vortex and 0 indicates no vortex as is shown in Figure 4.20. By finding the maximum swirl strength in the flow field the main vortex is able to be detected and its corresponding location is recorded at each time step.
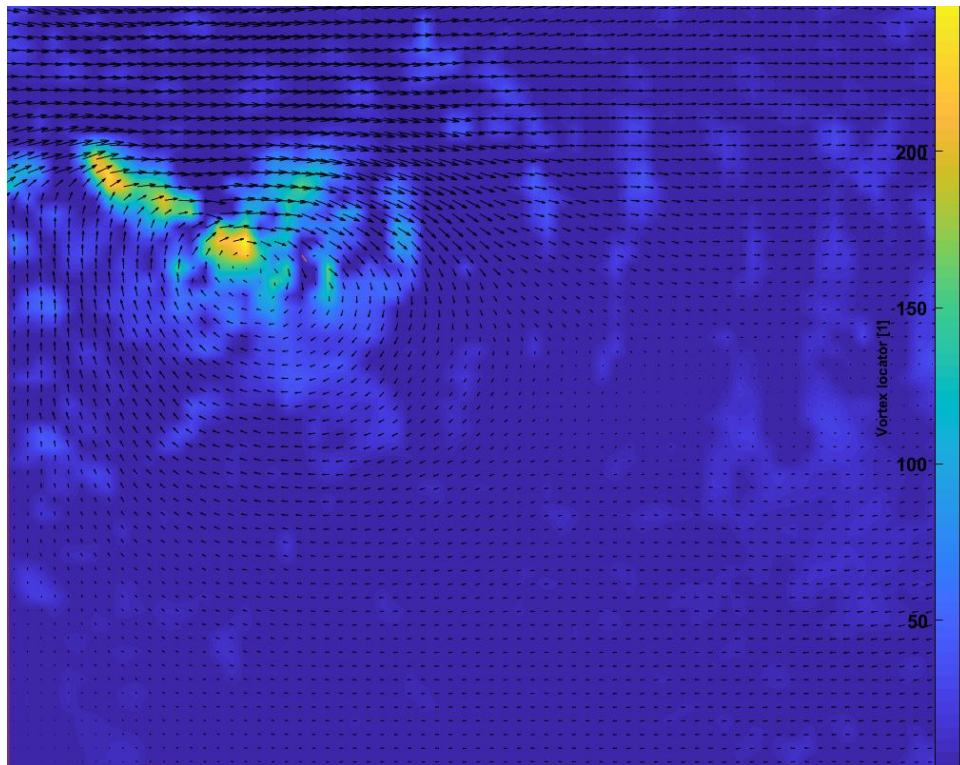
Figure 4.20: Vortex Locator Using Swirl Strength

5. RESULTS AND DISCUSSION

This chapter covers the results of the surface PIV analysis that was conducted for the vertical barrier island experiments. The first section will discuss the results of the flow rate analysis conducted to determine the accuracy of the pump in generating the desired flow rate for the experiments. This will be followed up with plots showing the trajectory and resulting behavior of the generated starting jet vortices in each of the 9 experimental configurations.

5.1 Summary of Experiment Conditions

In order to generate the desired vortex propagation behavior at the inlet, the period was set and the velocity was varied until critical conditions were observed. The experiments were conducted at three different water depths, 2 cm, 3 cm, and 5 cm. The entire set of experiments that were conducted is shown in Figure 5.1. Each of these cases will be identified and analyzed according to their respective water depth and K_w value.

Depth (cm)	U (m/s)	T (s)	K_w
2	0.02	66	0.35
2	0.04	66	0.20
2	0.08	98	0.07
3	0.04	66	0.20
3	0.06	66	0.13
3	0.08	66	0.10
5	0.05	66	0.17
5	0.05	66	0.15
5	0.07	98	0.07

Figure 5.1: Experiment Cases

5.2 Flow Rate Analysis

Following the Methodology in chapter 4.3.1.1, we were able to show that given a specific custom tidal flow signal, the ramp up and ramp down of the pump effectively modeled a sinusoidal tidal flow regime. This was true of all of the cases except for when the maximum flow rate for the experiment was below 5 GPM.

Figure 5.2 shows the 2 cm $K_w = 0.35$ experimental case where the data points did not allow for accurate fitting with a sinusoidal fit line. In Figure 5.2, the recorded data points are shown as black circles. The maximum flowrate during each tidal cycle that was recorded shows a steady decrease from approximately 3.25 GPM to about 2.5 GPM during the experiment. This may be explained by the gate valve that is used to set the maximum flowrate during each tidal cycle. With the gate valve fully open, the flowrate is approximately 110 GPM in the system. In order to create a maximum flowrate of less than 5 GPM the gate valve has to be almost shut such that the pressure against the gate is much larger than in the other experimental cases. This high pressure may be causing the gate to shift during each ramp up of the pump. At flowrates higher than 5 GPM, this shift in maximum flowrate was not observed.

Another Q was calculated by finding the cross-sectionally averaged velocity across the inlet found in the surface PIV analysis. The Q from the PIV measurements was then compared to the max Q recorded with the flow meter for comparison. To calculate the Q in the experiment, the cross-sectional area, A, of the inlet was applied such that $Q = UA$. The cross-sectionally averaged velocity as well as the corresponding Q values from the PIV analysis and the flow meter are shown in Figure 5.3.

Figure 5.3 shows that there is a non-negligible difference between the calculated Q using the surface cross-sectionally averaged surface velocity and the Q measured by the flow meter. The Q from the PIV analysis is consistently greater than 30% of the Q measured from the flow meter. By assuming the dynamics of the inlet to be similar to that of an open channel, we can assume that the boundary layer will be similar to that of an open channel such that the velocity will maintain a logarithmic profile with depth (White, 2011) as shown in Figure 5.4. This boundary layer may
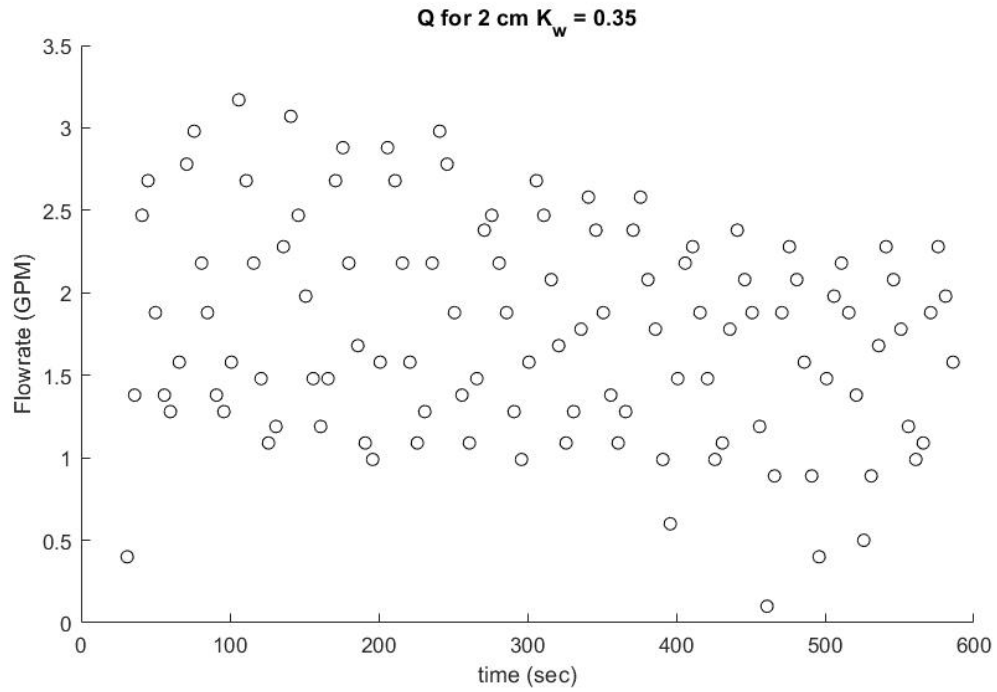
Figure 5.2: Q Measured from the Flow Meter for 2 cm $K_w = 0.35$ case

account for the difference in Q that we are recording from the flow meter and the Q found using the surface velocity at the inlet.

Depth (cm)	U (m/s)	T (s)	K_w	Q PIV	Q Flow Meter	% Difference
2	0.02	66	0.35	3.8	2.5	54
2	0.04	66	0.20	6.7	4.7	44
2	0.08	98	0.07	13.4	10.2	31
3	0.04	66	0.20	10.0	6.9	44
3	0.06	66	0.13	15.8	N/A	N/A
3	0.08	66	0.10	20.3	13.1	55
5	0.05	66	0.17	19.2	11.0	75
5	0.05	66	0.15	21.7	17.1	27
5	0.07	98	0.07	30.1	21.2	42

Figure 5.3: Values of U, T, K_w, Q from PIV, Q from Flow Meter, and the % Difference between Q PIV and Q Flow Meter for the Whole Set of Experiments
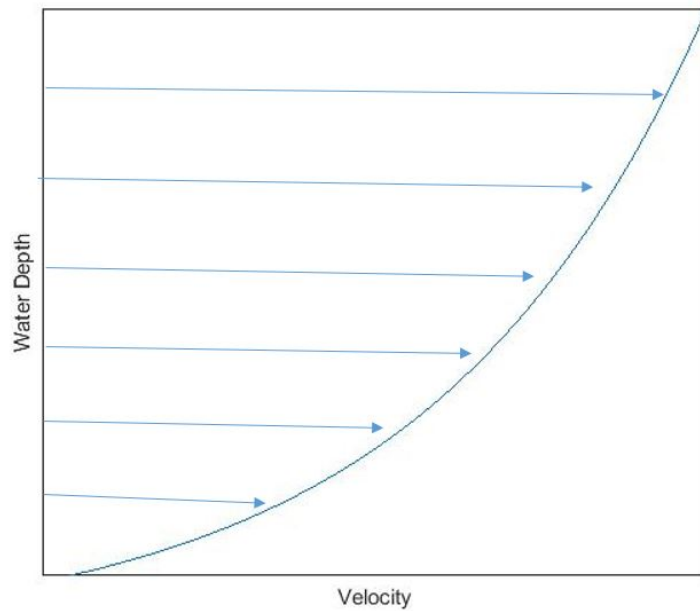
Figure 5.4: Example Logarithmic Boundary Layer Profile for an Open Channel

Non-Dimensional Variables
$x^* = \dfrac{x}{UT}\pi$
$y^* = \dfrac{y}{UT}\pi$
$t^* = \dfrac{tU}{W}$
$u^* = \dfrac{u}{U}$

Figure 5.5: Non-Dimensional Variables

5.3   Vortex Propagation

To analyze the propagation of the vortices, the relevant variables are non-dimensionalized for comparison to other experimental work. The list of non-dimensional parameters chosen is given in Figure 5.5. The x-direction is in the direction of the flow and the y-direction is in the direction of the side walls of the flume.

To determine the propagation behavior of the vortices, the swirl strength of the main vortex is tracked. Figure 5.6 shows the propagation of the vortex in the x^* and y^* directions as well as the non-dimensional inlet velocity, u^*, over time for the 2 cm $K_w = 0.35$ case. In this figure, the black vertical lines show the cut-off point between individual tidal cycles. These lines are defined at the zero upcrossing point for the averaged inlet velocity. Figures 5.7 and 5.8 show the vortex evolution over $0 - 0.5T$ and $0.6 - 0.9T$ respectively for the fourth tidal cycle to aid in the visualization of Figure 5.6. During $0 - 0.4T$, a small vortex forms on the edge of the barrier island but as soon as the tide begins to reverse at $0.5T$, the vortex begins to lose coherence and is entrained back through the inlet. The vortex that is shown in this case is weaker than in most of the other experimental cases due to the decreasing flow rate each tidal cycle. This is most likely due to the issues with the gate valve that were previously identified.

Figure 5.9 shows the propagation behavior and u^* for the 2cm $K_w = 0.2$ case. In Figures 5.10
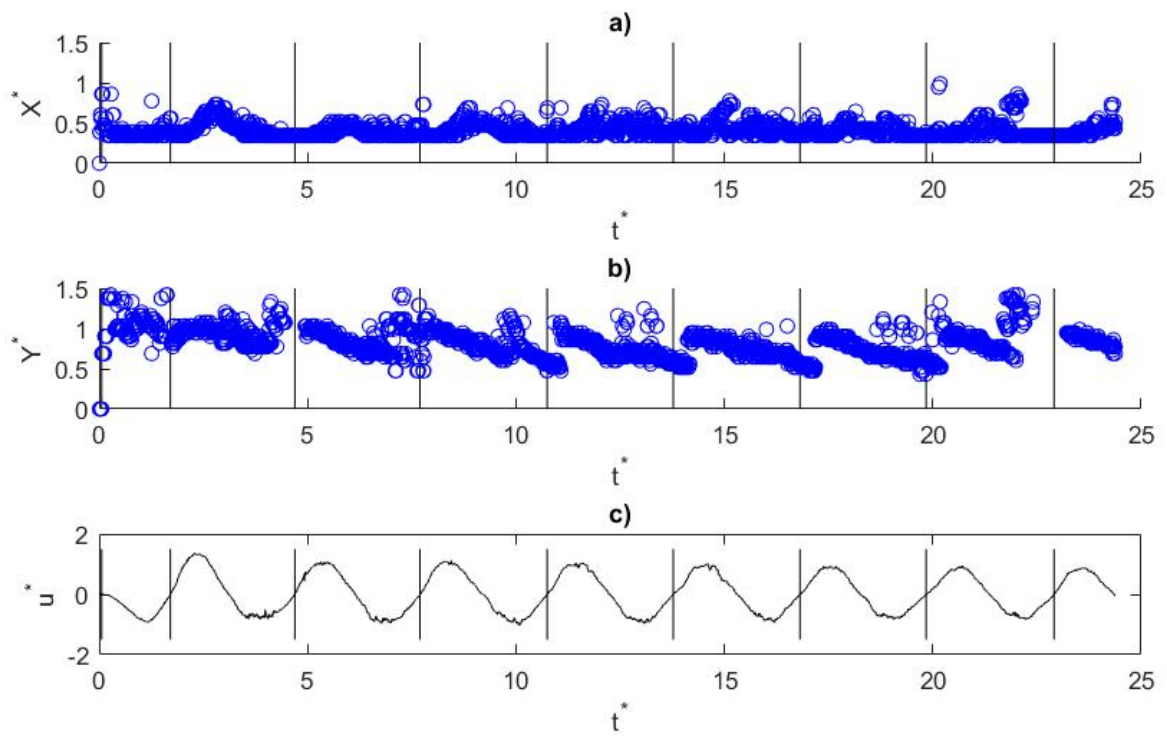
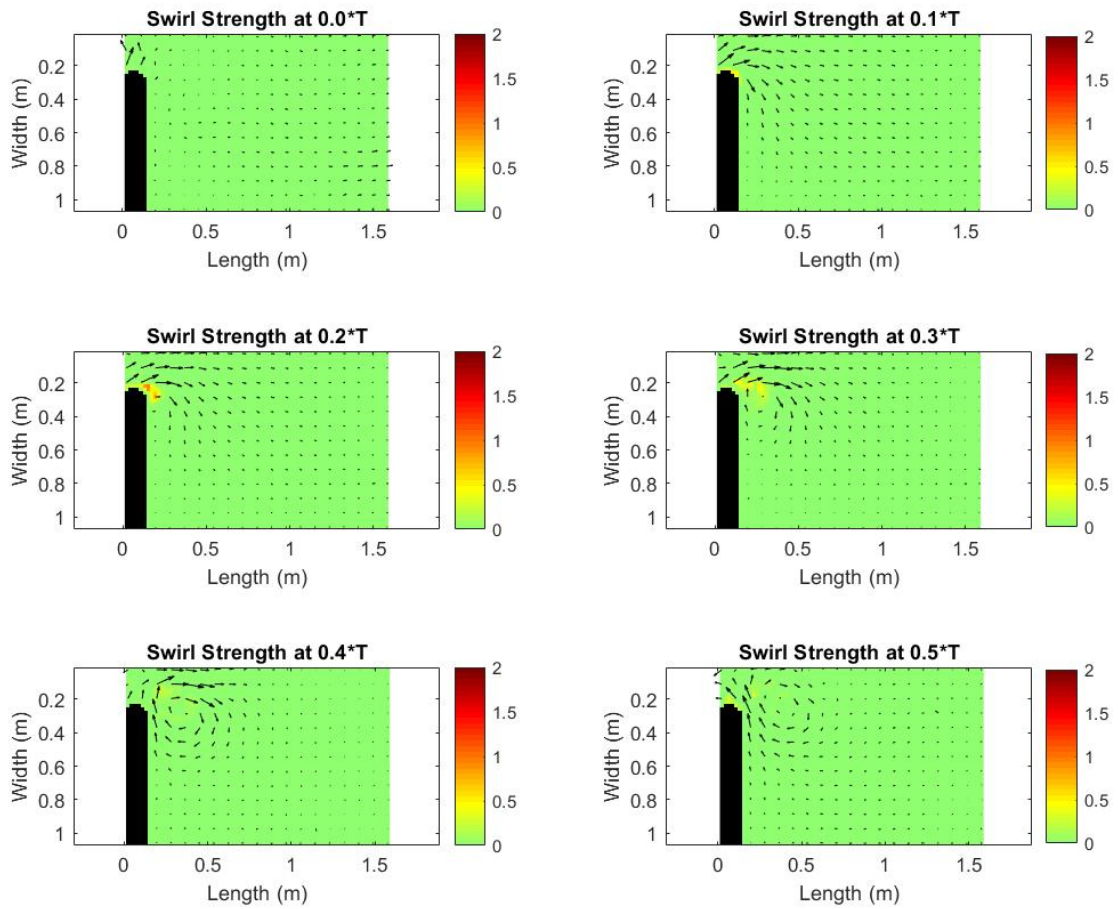Figure 5.6: Vortex Tracking 2cm Kw = 0.35: a) x^* vs t^*, b) y^* vs t^*, c) u^* vs t^*

Figure 5.7: 2cm Kw = 0.35 Vortex Evolution over 0-0.5T for Tidal Cycle 4
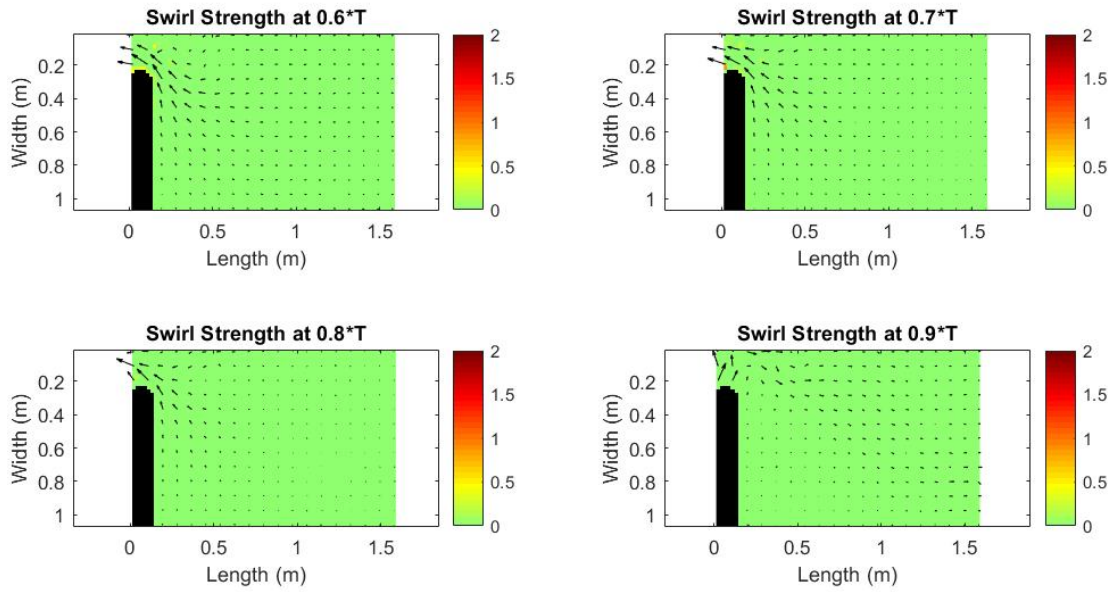
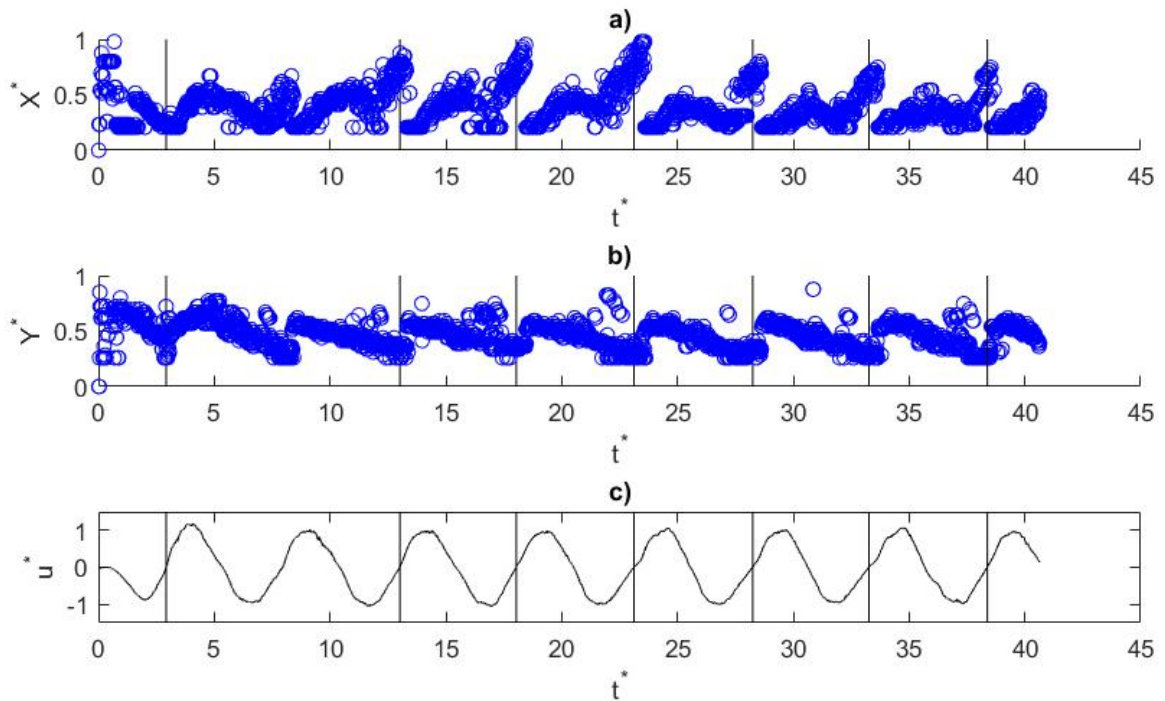Figure 5.8: 2cm Kw = 0.35 Vortex Evolution over 0.6-0.9T for Tidal Cycle 4

Figure 5.9: Vortex Tracking 2cm Kw = 0.2: a) x^* vs t^*, b) y^* vs t^*, c) u^* vs t^*

and 5.11, a visualization of the propagation for tidal cycle 5 is shown. In this case, the K_w value of 0.2 suggests that the vortex will entrain back into the inlet, which is what is observed during the tidal cycle. After the major vortex is entrained into the inlet, a small part of the larger vortex manages to survive until slack tide. This is why there is a jump up in the x^* plot in Figure 5.9 where the surviving part of the vortex is identified as the main vortex.

The 2 cm K_w = 0.07 case does not behave exactly as is expected as shown in Figure 5.12. In cycles 2 and 5, there is behavior other than the propagation away behavior that is expected. Figures 5.13 and 5.14 show the propagation behavior during the fourth tidal cycle. The vortex appears to lose coherency after $0.5T$ in the tidal cycle and since the l_t/l_f ratio is higher for the 2cm case than for the deeper cases it may explain why the vortex loses coherency such that the tracking algorithm has issues following it correctly during some of the tidal cycles. Even though the tracking algorithm has issues determining the center of the vortex after $0.5T$, there is still a
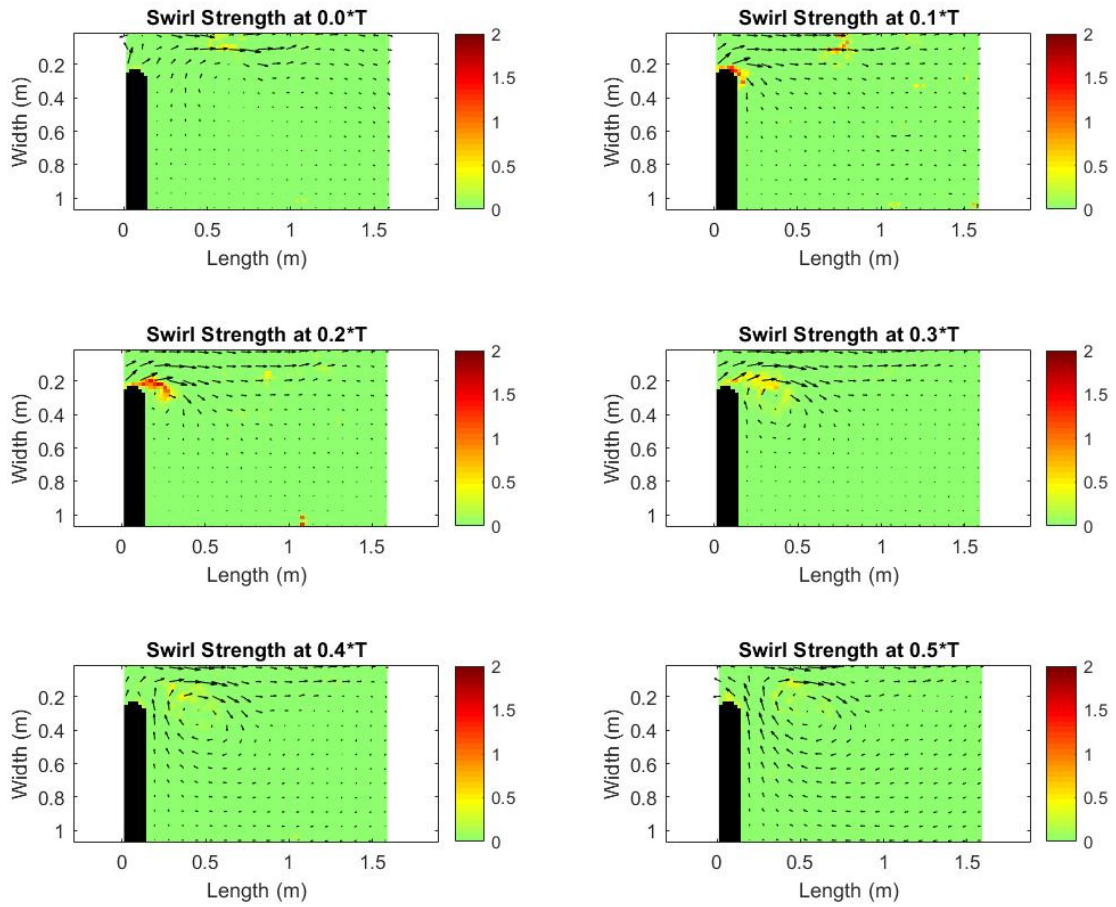
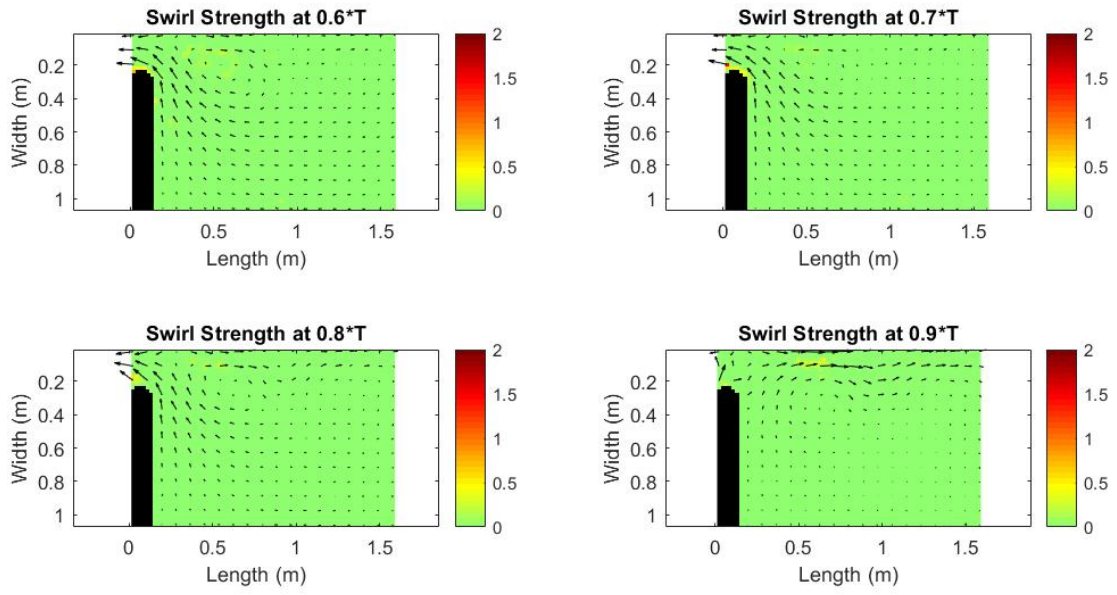Figure 5.10: 2cm Kw = 0.2 Vortex Evolution over 0-0.5T for Tidal Cycle 5

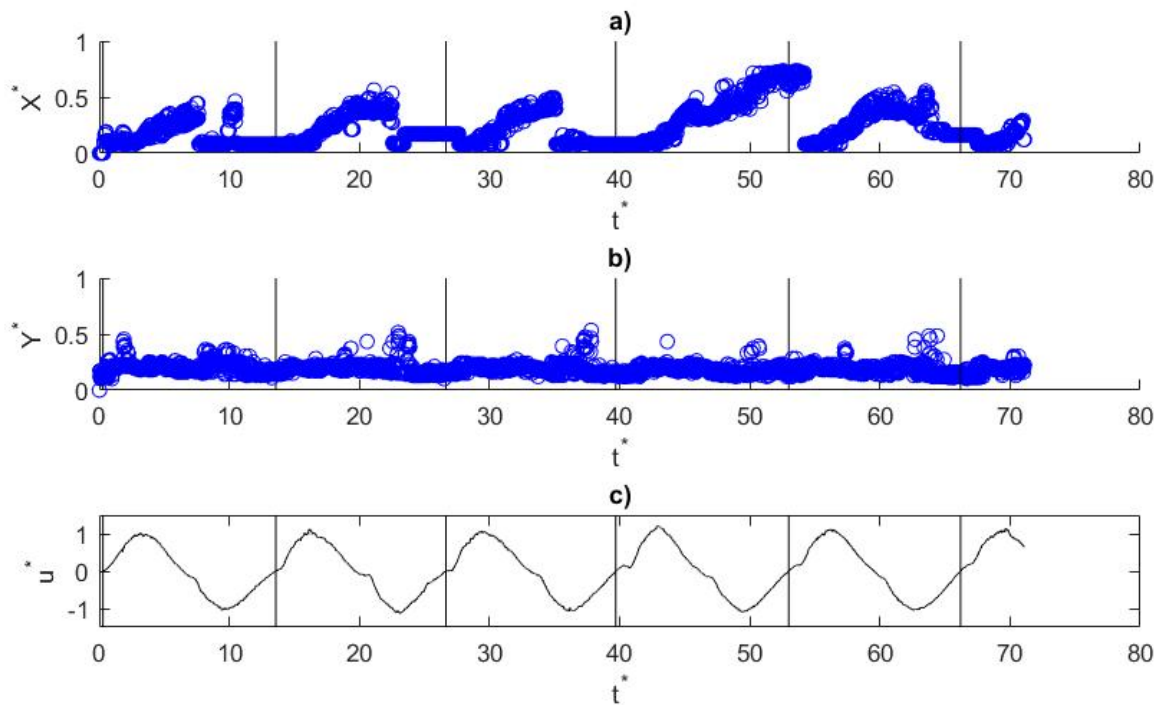Figure 5.11: 2cm Kw = 0.2 Vortex Evolution over 0.6-0.9T for Tidal Cycle 5

Figure 5.12: Vortex Tracking 2cm Kw = 0.07: a) x^* vs t^*, b) y^* vs t^*, c) u^* vs t^*

clearly visible vortex that continues to propagate away from the inlet during the tidal cycle.

The 3 cm $K_w = 0.20$ case showed the expected vortex entrainment during the experiments. Figure 5.15 shows the detailed propagation information from the vortex tracking algorithm and associated averaged inlet velocity during the tidal cycles. Figures 5.16 and 5.17 show the plotted swirl strength for tidal cycle 5. The vortex begins to form and propagate to approximately $x = 0.5$m by tidal cycle $0.5T$, but then the flow reverses and the vortex loses swirl strength and begins to be pulled back towards the inlet until there is almost no swirl strength left.

For the 3cm $Kw = 0.13$ case, the expected behavior is that the vortices will maintain position during the tidal cycle. Figure 5.18 shows that for most cycles the vortex becomes stuck at around $x^* = 0.5$ during the reversing tide then propagates as the inlet reversing tide decreases. A visualization of this behavior during tidal cycle 4 is shown in Figures 5.19 and 5.20. At the beginning of the cycle, the remnants of the last cycles vortex remains in the right side of the plots. Once the
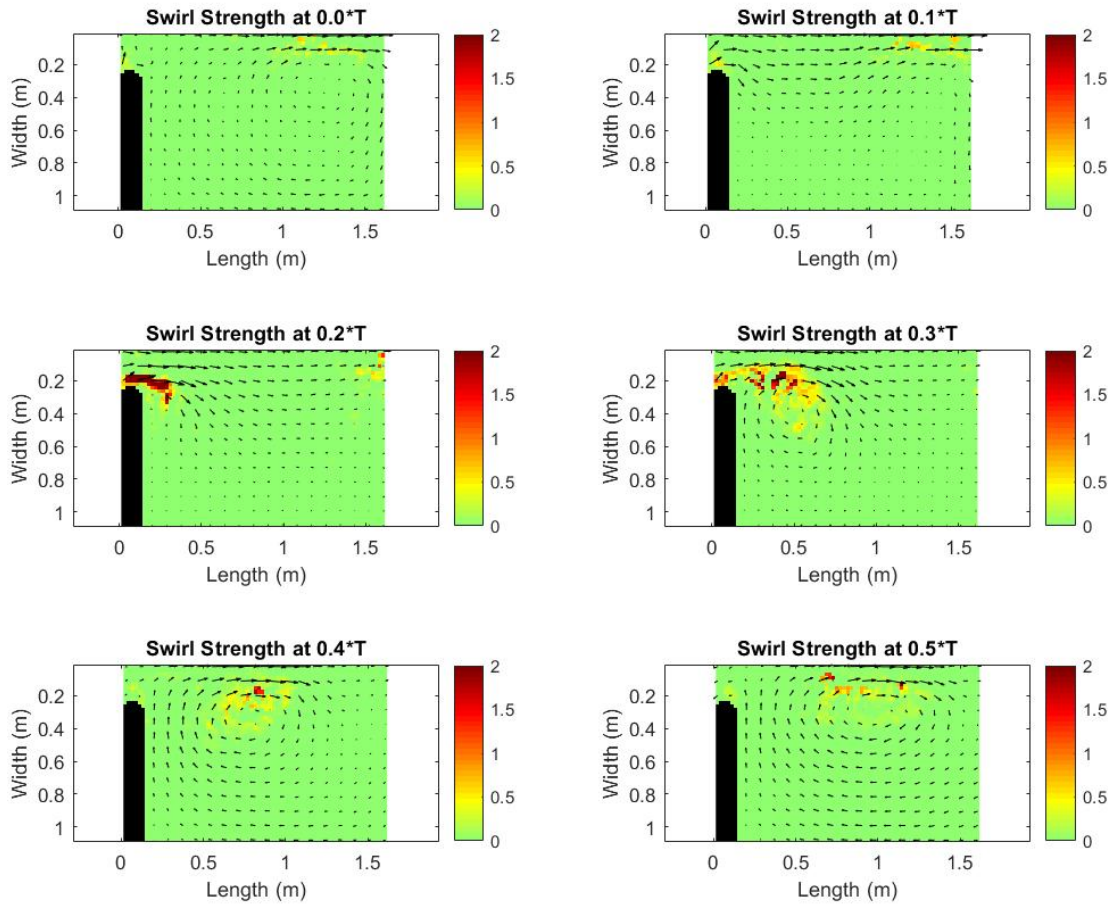
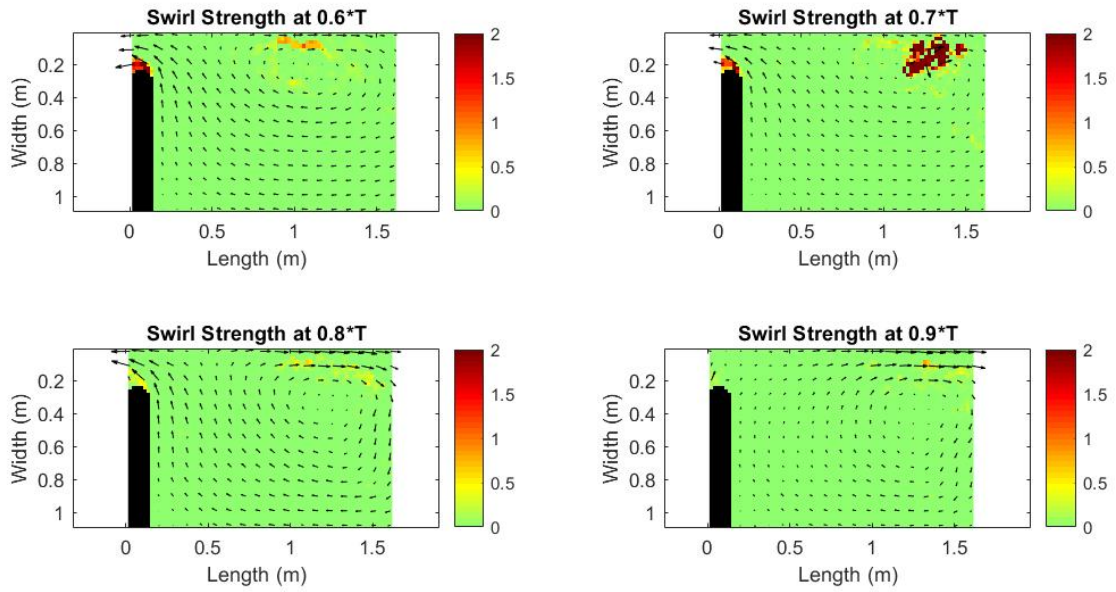Figure 5.13: 2cm Kw = 0.07 Vortex Evolution over 0-0.5T for Tidal Cycle 4

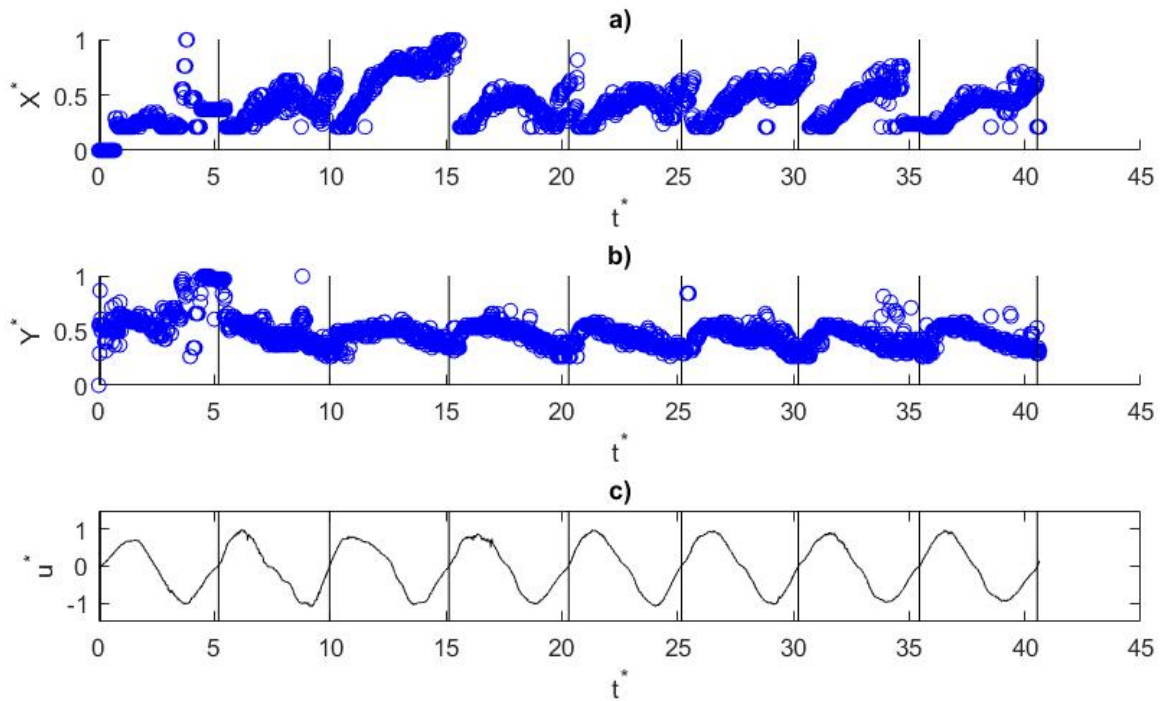Figure 5.14: 2cm Kw = 0.07 Vortex Evolution over 0.6-0.9T for Tidal Cycle 4

Figure 5.15: Vortex Tracking 3cm Kw = 0.20: a) x^* vs t^*, b) y^* vs t^*, c) u^* vs t^*

vortex begins to form it propagates to approximately $x = 0.75$m where it remains until $0.9T$ when it begins to propagate forward due to the reversing current approaching zero.

The 3cm $K_w = 0.10$ case shows a distinctly different behavior than for the previous two 3 cm water depth cases as is shown in Figure 5.21. In this experiment, the vortices always propagate through the reversing tide and continue until the next cycle begins. An example of this behavior is shown for tidal cycle 5 in Figures 5.22 and 5.23. During tidal cycle 5, it is clear to see that the vortex continues moving further in the x-direction during each proceeding time step.
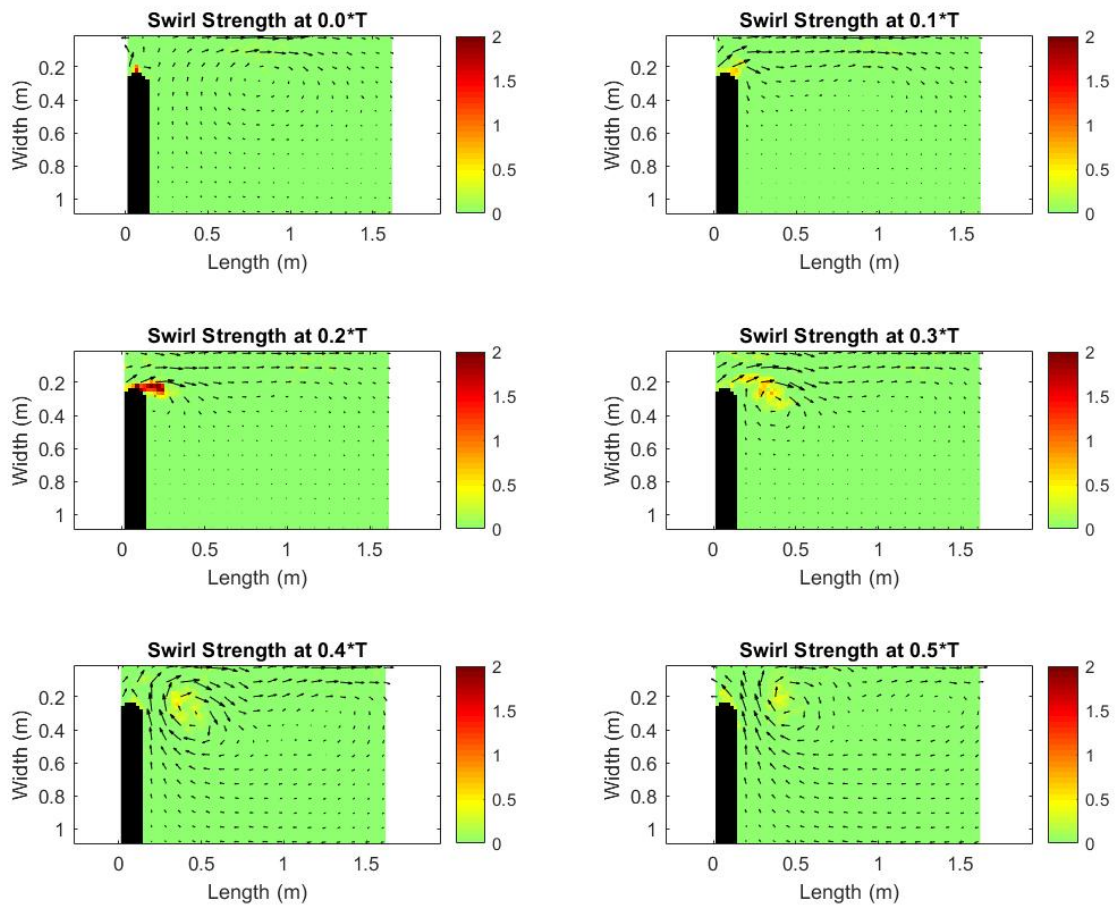
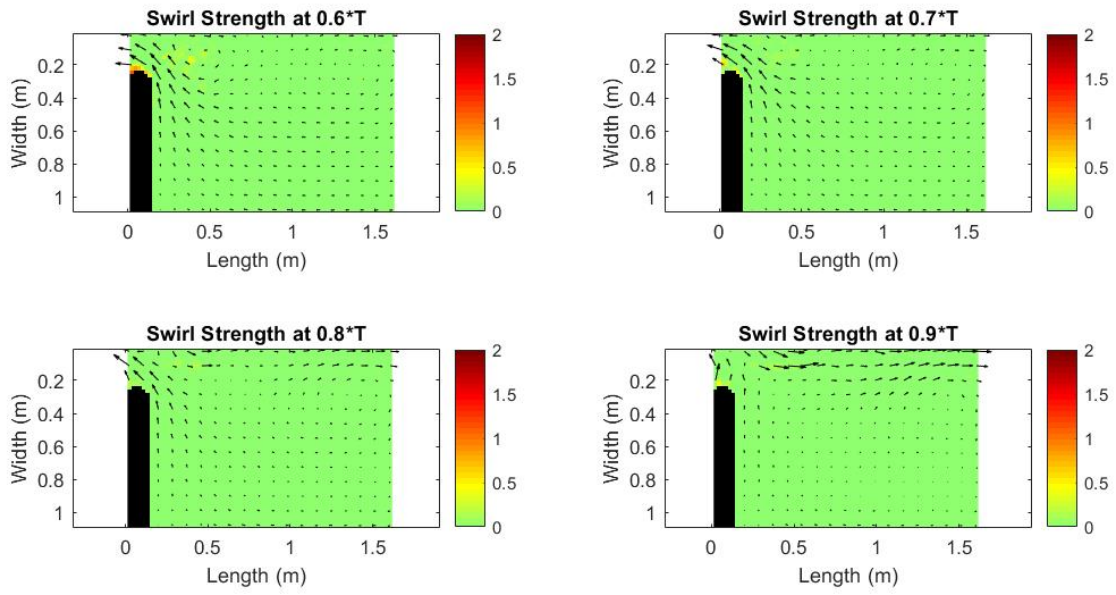Figure 5.16: 3cm Kw = 0.20 Vortex Evolution over 0-0.5T for Tidal Cycle 5

Figure 5.17: 3cm Kw = 0.20 Vortex Evolution over 0.6-0.9T for Tidal Cycle 5

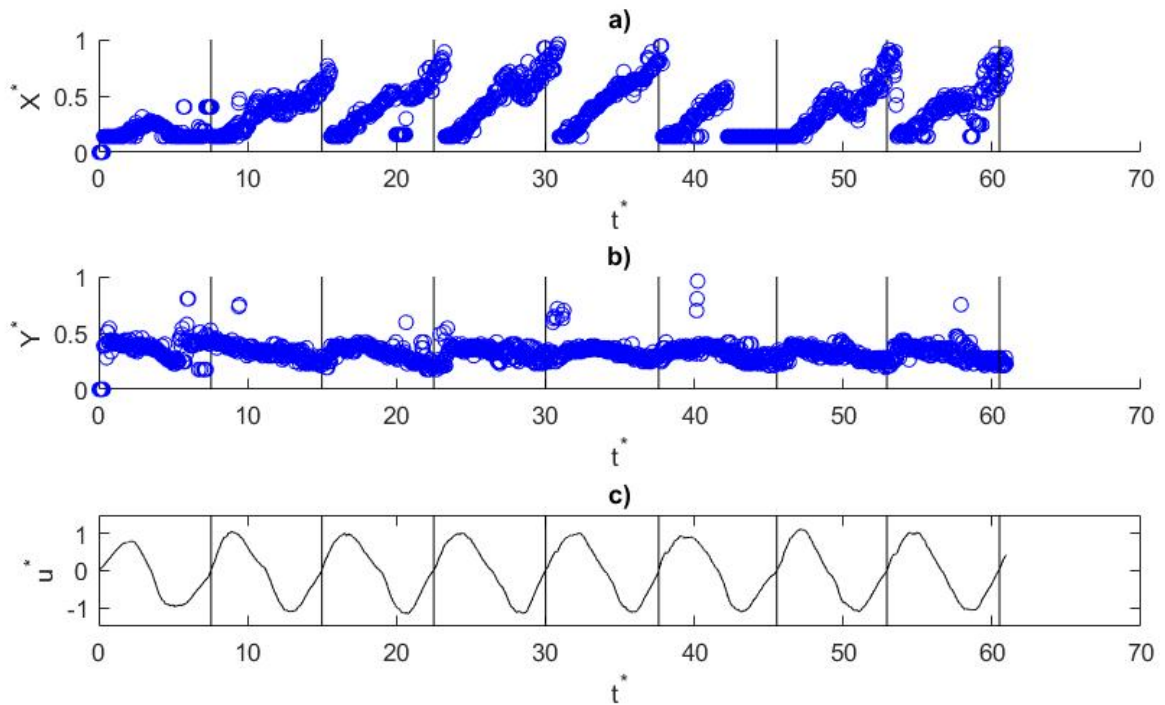Figure 5.18: Vortex Tracking 3cm Kw = 0.13: a) x^* vs t^*, b) y^* vs t^*, c) u^* vs t^*

The 5 cm cases show an interesting phenomena that the 2cm and 3cm cases did not have. By looking at Figure 5.24 for the 5 cm $K_w = 0.18$ case, resonance can be seen in the velocity plot where there are multiple local minimums and maximums during each tidal cycle. Figure 5.25 and 5.26 show the vortex evolution over tidal cycle 7. Even though there is recorded resonance occurring in the inlet velocity data, there is still the expected vortex entrainment behavior indicated by the K_w value.
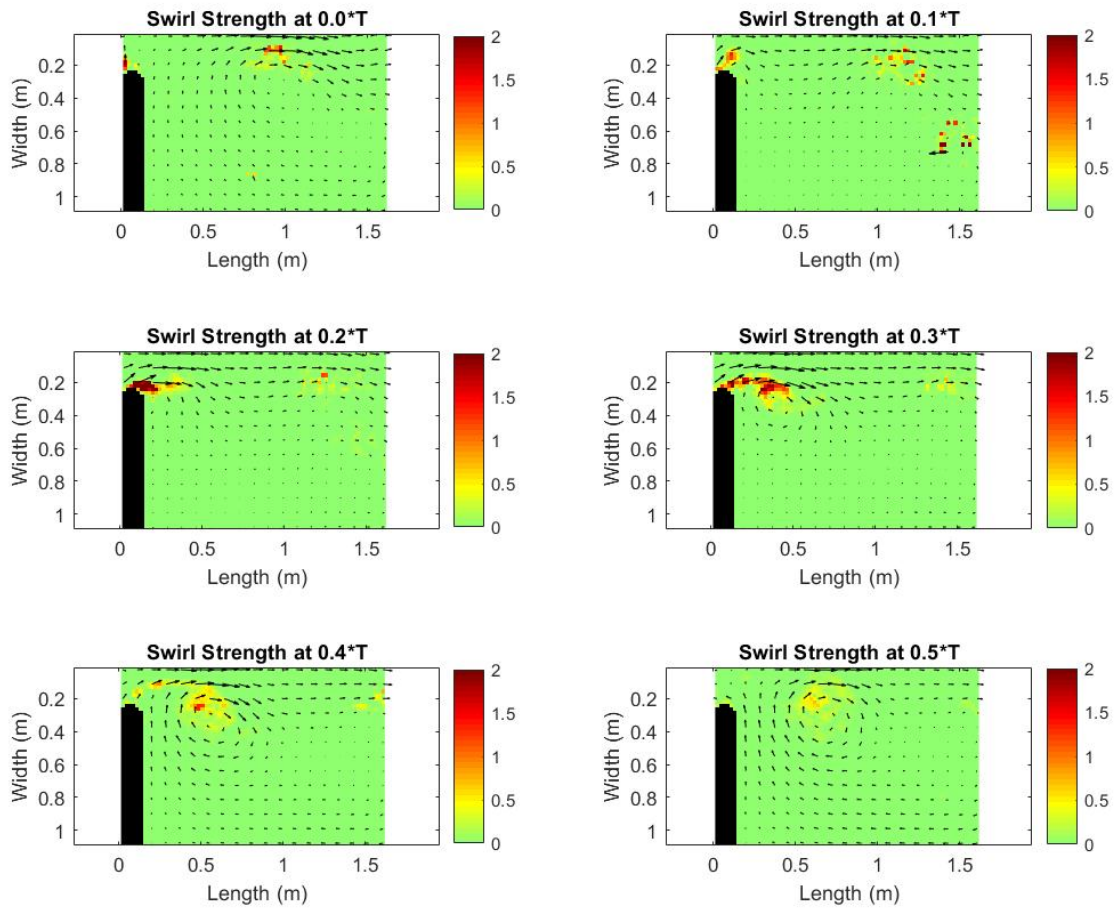
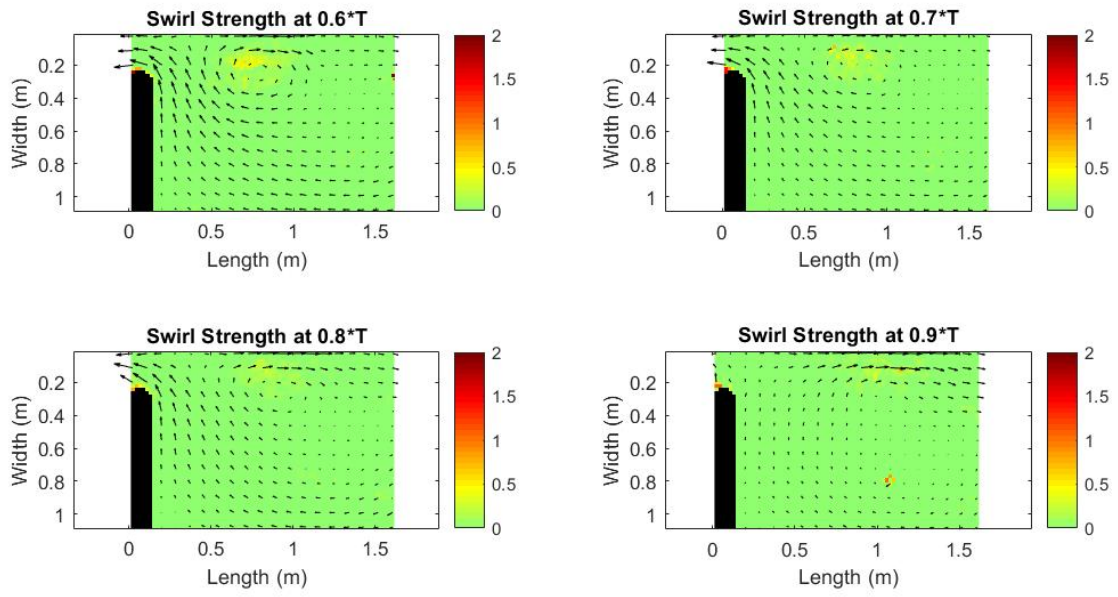Figure 5.19: 3cm Kw = 0.13 Vortex Evolution over 0-0.5T for Tidal Cycle 4

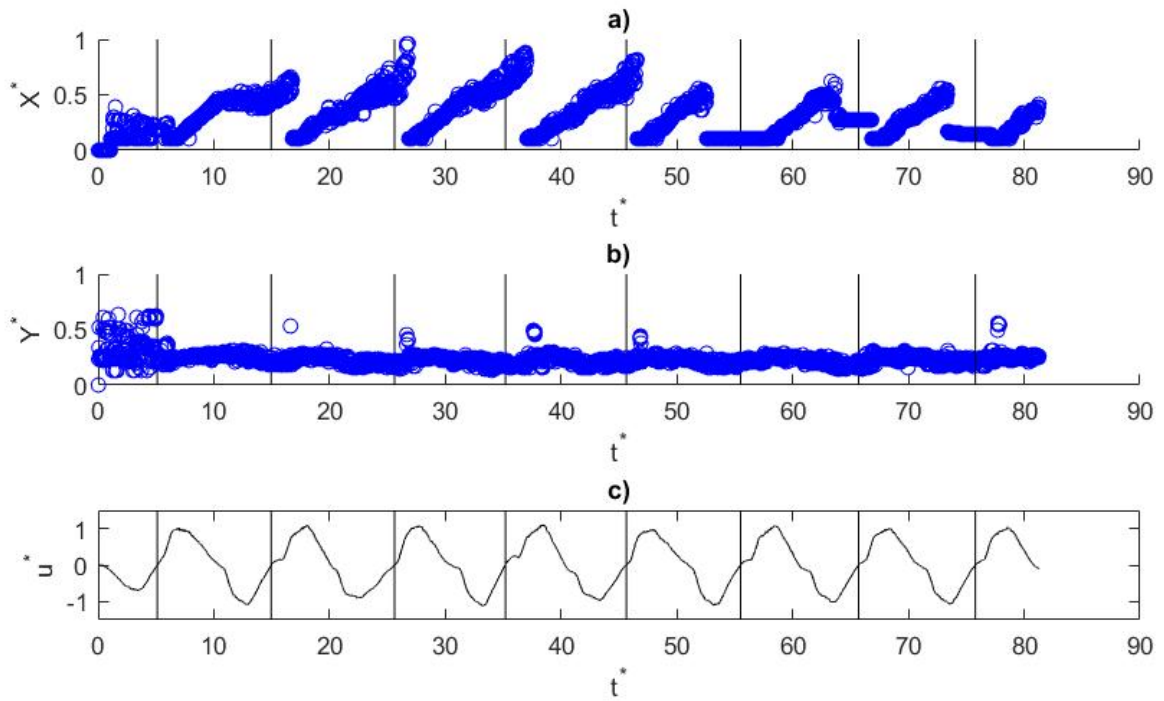Figure 5.20: 3cm Kw = 0.13 Vortex Evolution over 0.6-0.9T for Tidal Cycle 4

Figure 5.21: Vortex Tracking 3cm Kw = 0.10: a) x^* vs t^*, b) y^* vs t^*, c) u^* vs t^*

Figure 5.27 shows the corresponding velocity propagation and velocity information for the 5 cm $K_w = 0.15$ case. There is also resonance recorded in this case similar to what was recorded in the 5 cm $K_w = 0.18$ case. Figures 5.28 and 5.29 show the vortex propagation over tidal cycle 4. The behavior is as expected for a K_w value close to 0.13 where the vortex propagates to about $x = 0.75$ by $0.5T$ and remains there until approximately $0.9T$. There is a noticeable difference in this case than in the previous critical condition experiments in the 2 cm and 3 cm cases. At $0.4T$, there is clearly a large secondary vortex forming behind the main vortex that is not seen in previous cases. By analyzing the velocity information for tidal cycle 4 in Figure 5.27, two peak velocities occur during the tidal cycle. This may be what is causing the formation of the large secondary vortex that is not seen in the previous cases.

The last case analyzed is the 5 cm $K_w = 0.08$ condition. Figure 5.30 shows the detailed propagation and velocity information for this experiment case. There are multiple local minimum and
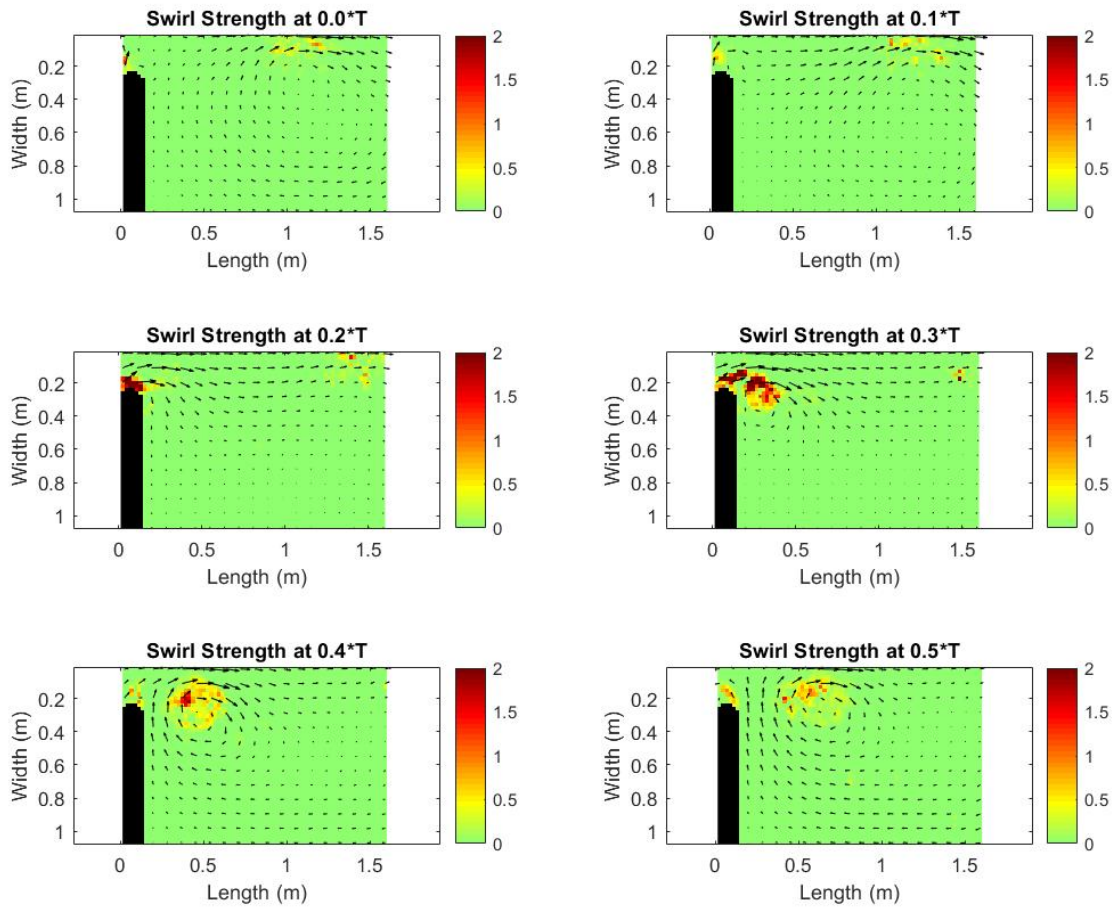
71

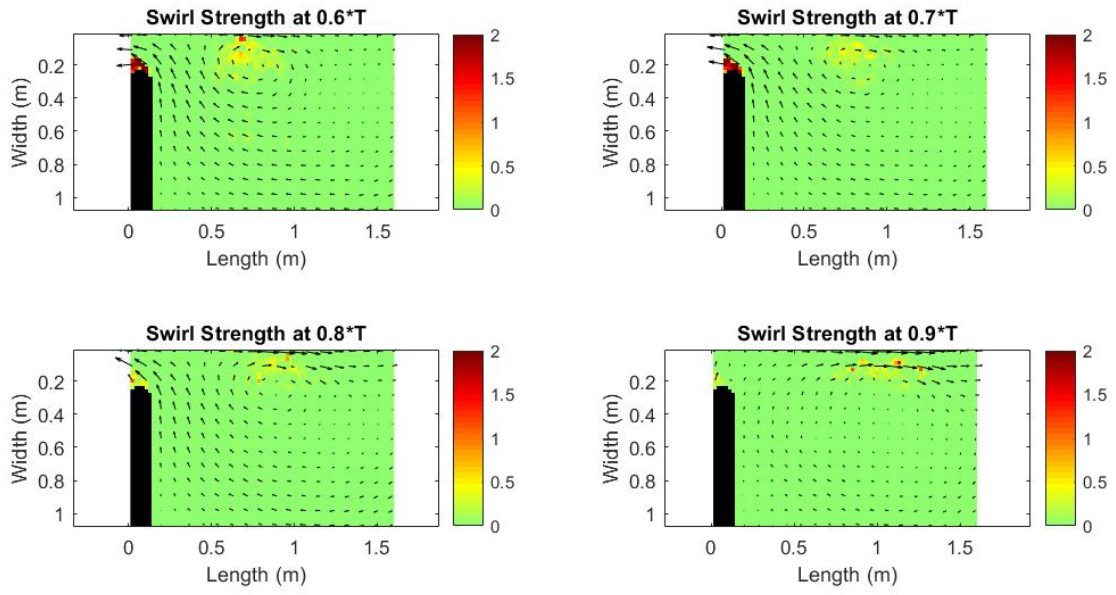Figure 5.22: 3cm Kw = 0.10 Vortex Evolution over 0-0.5T for Tidal Cycle 5

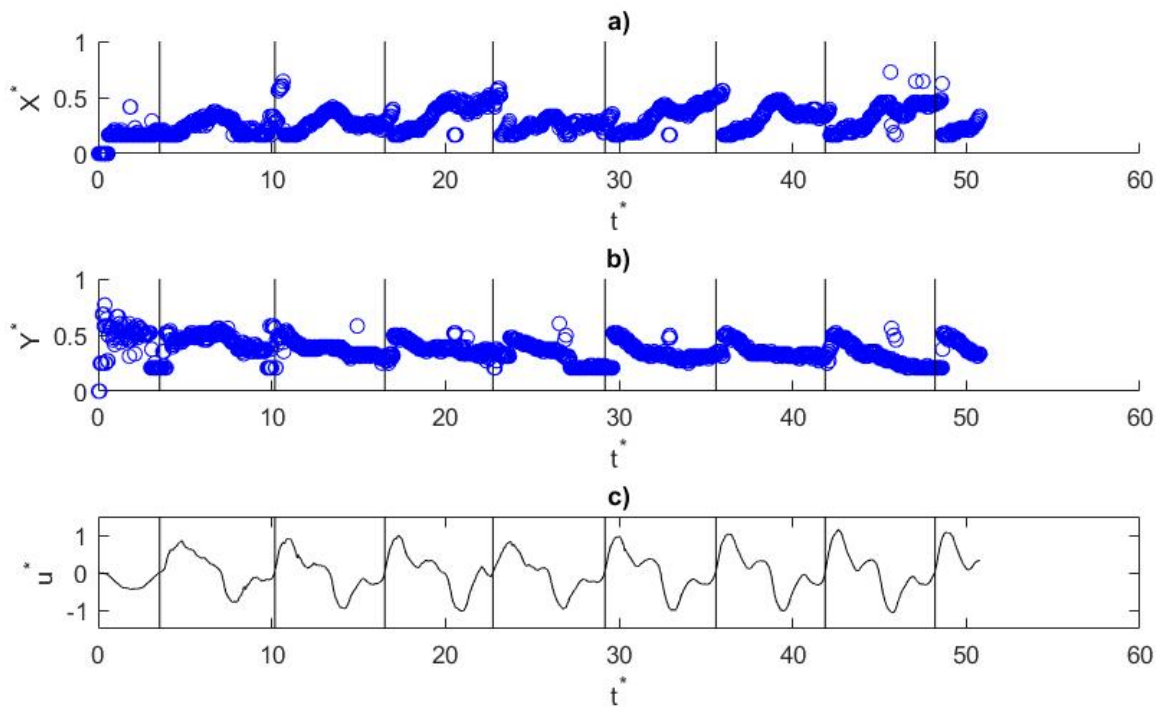Figure 5.23: 3cm Kw = 0.10 Vortex Evolution over 0.6-0.9T for Tidal Cycle 5

Figure 5.24: Vortex Tracking 5cm Kw = 0.18: a) x^* vs t^*, b) y^* vs t^*, c) u^* vs t^*

maximum velocities during each tidal cycle. Figures 5.31 and 5.32 show that the vortex evolution over tidal cycle 3 displays the expected behavior, in which, the vortex propagates further in the x-direction during each proceeding frame. Similar to what was observed in the 5 cm $K_w = 0.15$ case, clear secondary vortices are forming at $0.4T$ that may be the result of the observed velocity fluctuations during the tidal cycle.

Figure 5.25: 5cm Kw = 0.18 Vortex Evolution over 0-0.5T for Tidal Cycle 7

Figure 5.26: 5cm Kw = 0.18 Vortex Evolution over 0.6-0.9T for Tidal Cycle 7

Figure 5.27: Vortex Tracking 5cm Kw = 0.15: a) x^* vs t^*, b) y^* vs t^*, c) u^* vs t^*

Figure 5.28: 5cm Kw = 0.15 Vortex Evolution over 0-0.5T for Tidal Cycle 4

Figure 5.29: 5cm Kw = 0.15 Vortex Evolution over 0.6-0.9T for Tidal Cycle 4

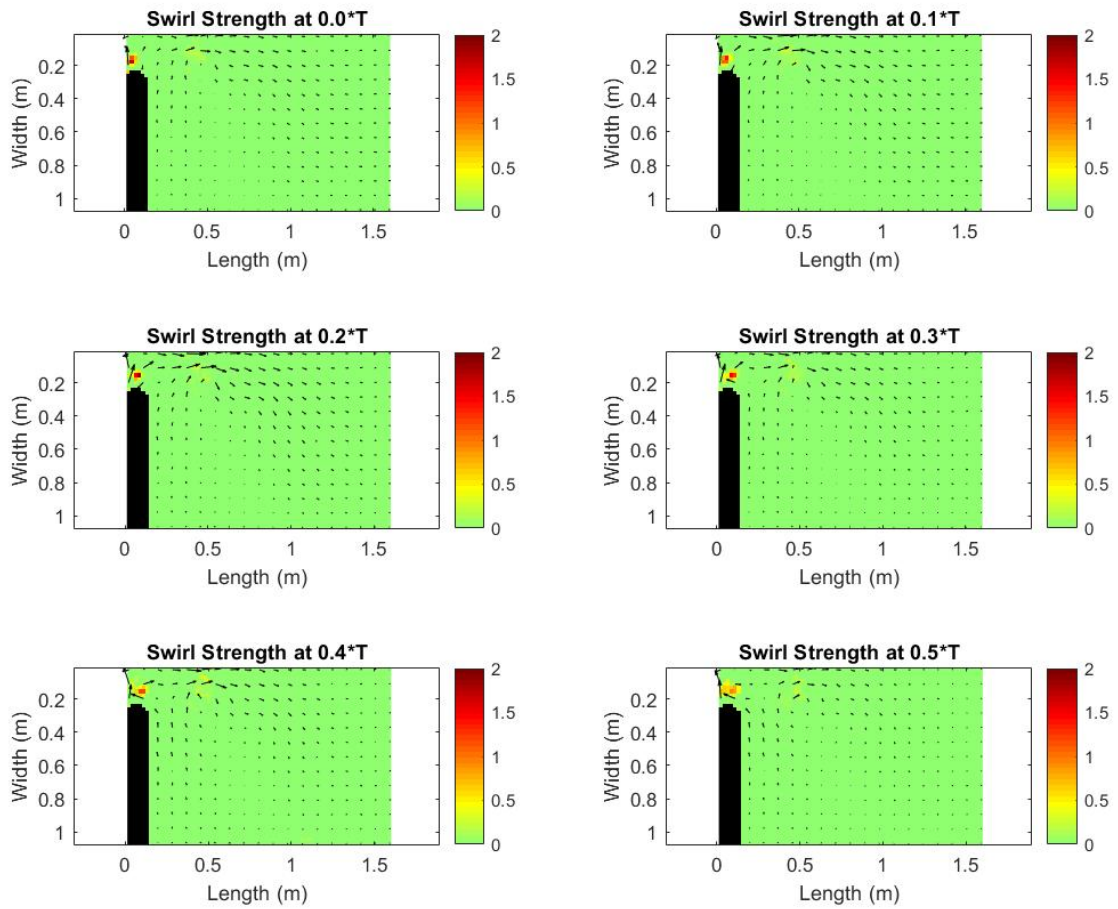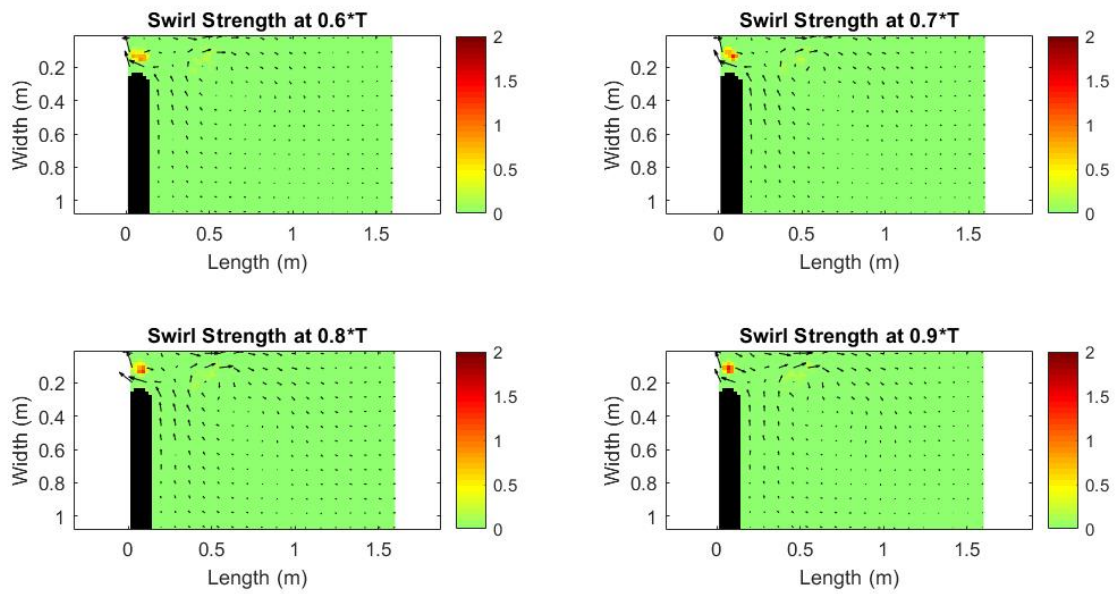Figure 5.30: Vortex Tracking 5cm Kw = 0.08: a) x^* vs t^*, b) y^* vs t^*, c) u^* vs t^*

Figure 5.31: 5cm Kw = 0.08 Vortex Evolution over 0-0.5T for Tidal Cycle 3

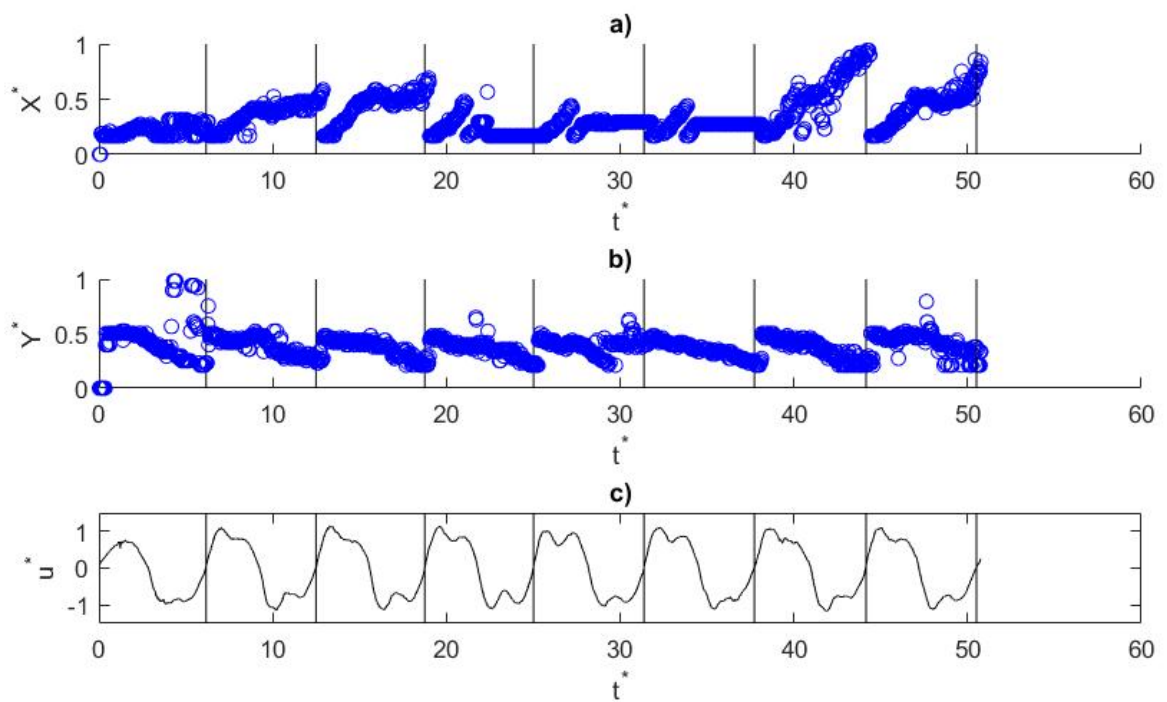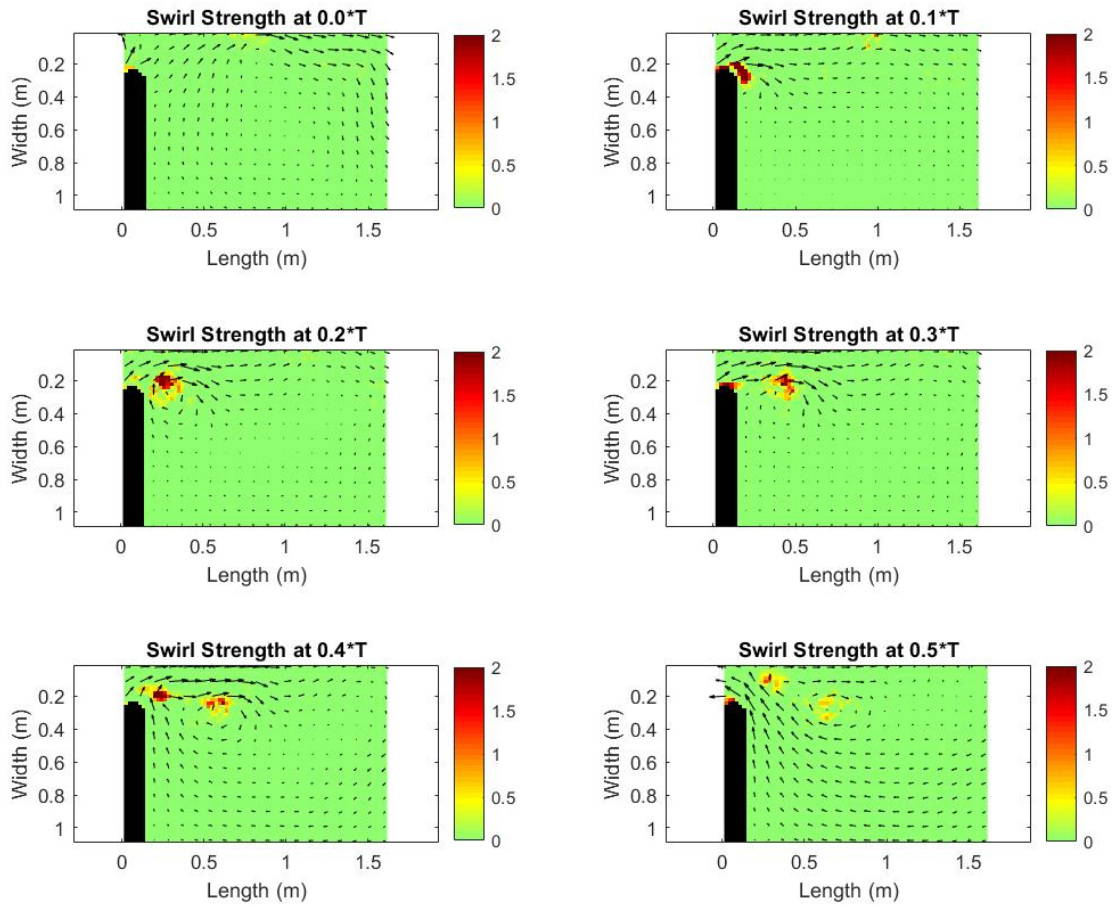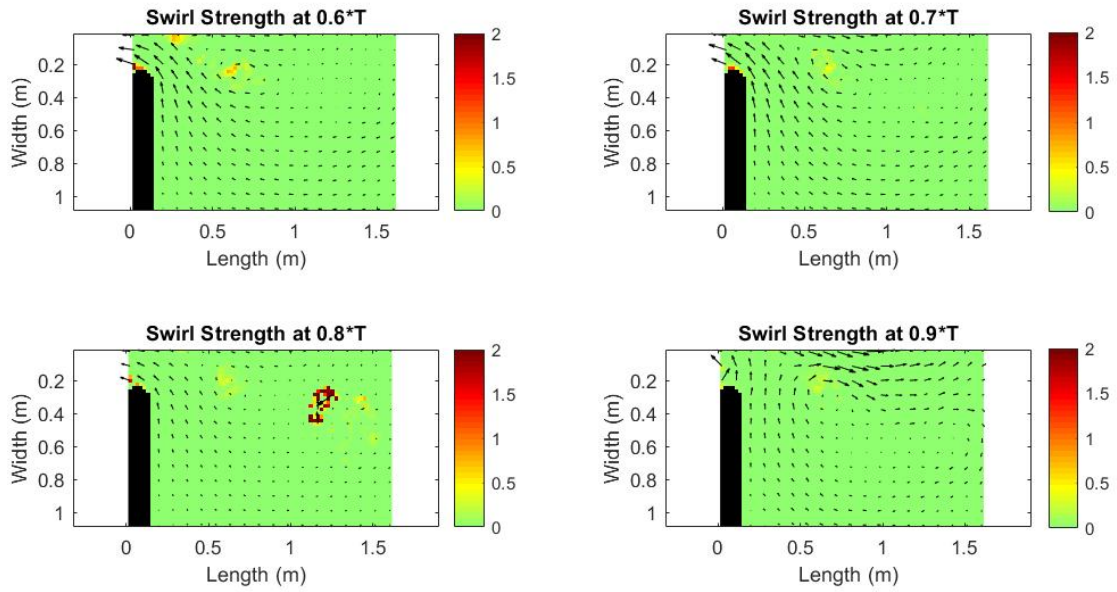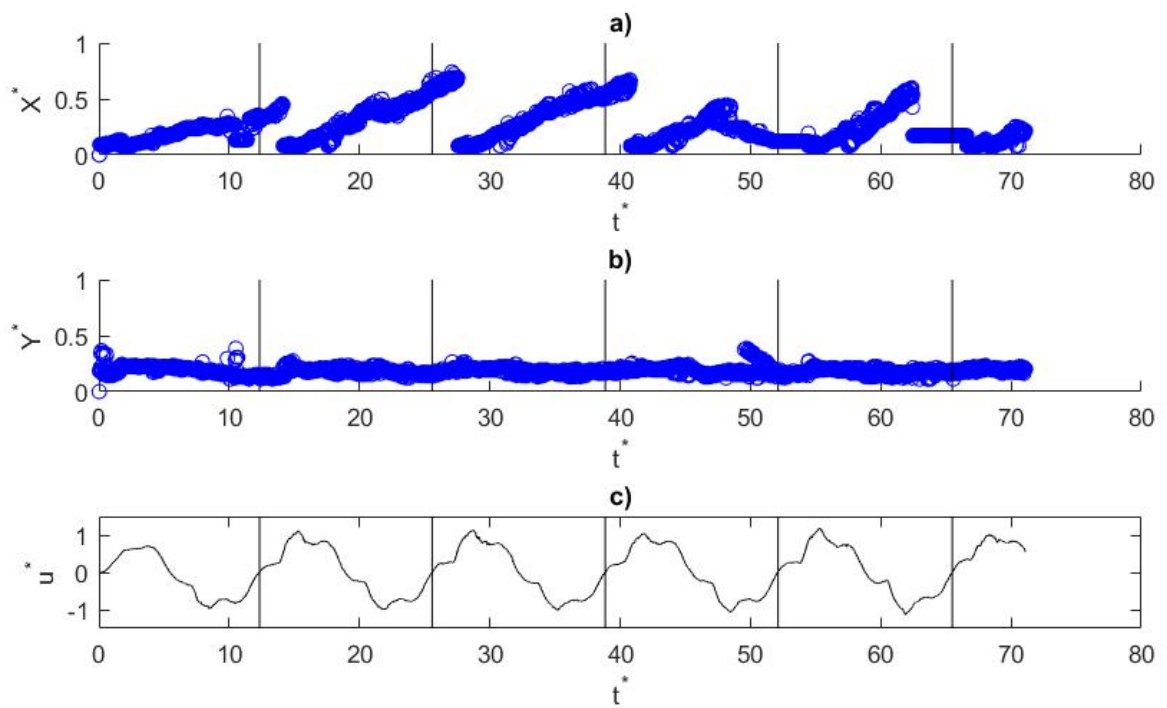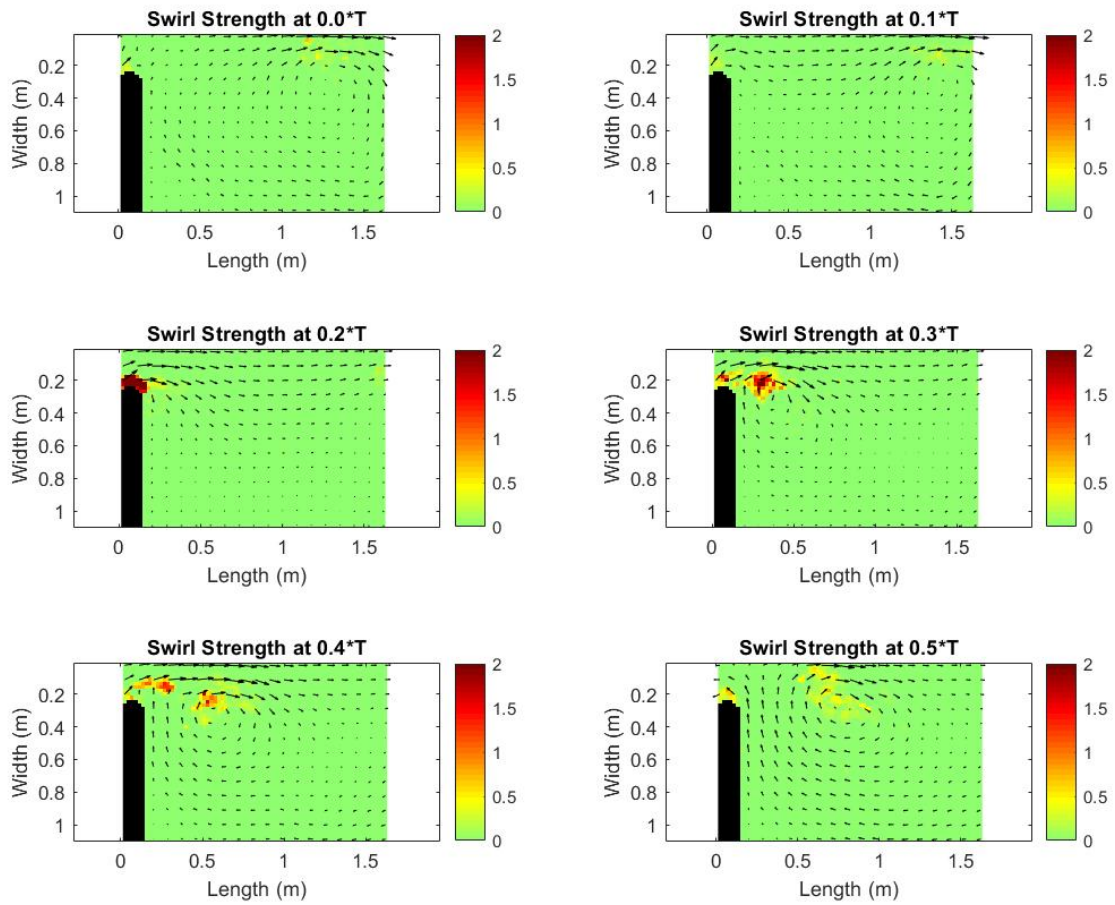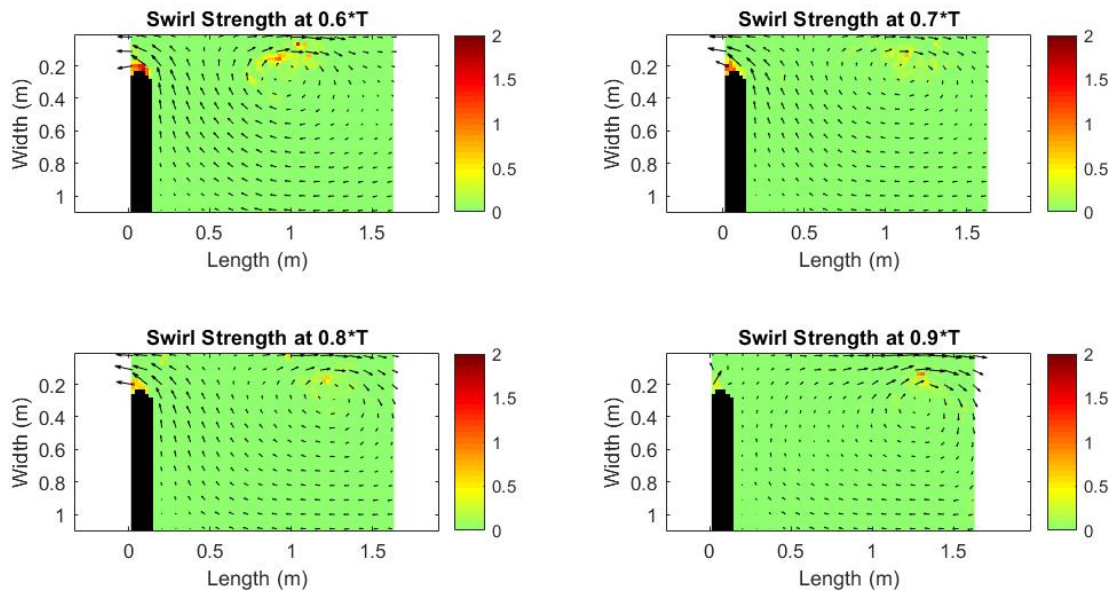Figure 5.32: 5cm Kw = 0.08 Vortex Evolution over 0.6-0.9T for Tidal Cycle 3

6.   CONCLUSIONS AND RECOMMENDATIONS

In this report, a shallow water flume was designed based on developing a method for utilizing the critical non-dimensional space to size the flume. Several calculations were conducted to try to ensure the hydrodynamic uniformity of the flume, and the flume equipment was calibrated for future experiments. Following a similar methodology to past starting jet vortex experiments, experiments were conducted in the flume to validate the performance of the new flume.

The methodology presented for designing the flume was shown to work by developing vortex behavior as predicted in past experiments. Another critical component to designing a new flume is understanding the limitations of what materials and equipment are available. For this design process, the flume was designed around standard 4ft x 8ft tempered glass sheets that are ready in mass availability. By incorporating the standard sizings for equipment into the design process, there were many more opportunities to adjust designs as the experiments progressed which allowed us to conduct more experiments in a faster time than most larger flumes allow. Designing around readily available equipment is something that should definitely be considered during the design process to have the most optimal design.

To calculate and understand the hydrodynamic conditions for the flume, several steps were taken. First, the uniformity of the flow field with the line diffuser, rubberized hair, and flow straighteners were visualized with dye. The visualization allowed for qualitative assessments about the uniformity to be made, followed by quantitative assessment and analysis to document any of the irregularities in the flow field. Then, testing of the pump and variable frequency drive system was conducted to determine the pump's ability to accurately simulate a tidal flow pattern. The data recorded from the flow meter for the pump performance during experiments was fitted with a non-linear regression, and the fit showed that the pump is behaving consistently with the sinusoidal signal that was generated to simulate tidal flow. After the pump analysis, collected data showed that the flowrate measured by the flow meter was consistently lower than the flowrate calculated from the surface PIV. This was thought to be due to the open channel boundary layer that is formed

in the inlet, so there will need to be some consideration given to the depth and cross-sectionally averaged velocity used for the inlet in future experiments.

The experiments conducted showed good agreement with the expected behavior of the vortices for the different depth and K_w conditions. As was expected, vortices that were generated in an experiment with approximately the value of $K_w = 0.13$ were getting trapped in the reversing tide, vortices with lower K_w values were propagating away, and vortices with higher K_w values were being entrained into the inlet during the reversing tide. There appeared to be some resonance in the 5 cm water depth cases that caused some abnormalities in the data that need to be taken into consideration during future experiments.

6.1   Future Work

The next steps to advance this research would be to conduct experiments more closely aligned with the observed conditions of an actual tidal inlet such as the Galveston bay inlet. We could do this by increasing the width of the flume from the 0.527 m inlet used in these experiments to 0.7 m. By conducting experiments at $K_w = 0.11$ so that we have propagation behavior as was expected in our January 2018 current buoy data for the Galveston bay inlet, we could run experiments in the new parameter space shown in Figure 6.1. This new parameter space would allow us to select experiments where frictional effects would be more significant. By conducting experiments with significant frictional effects we could help elucidate the role that bottom friction has on the propagation and formation of tidal vortices.
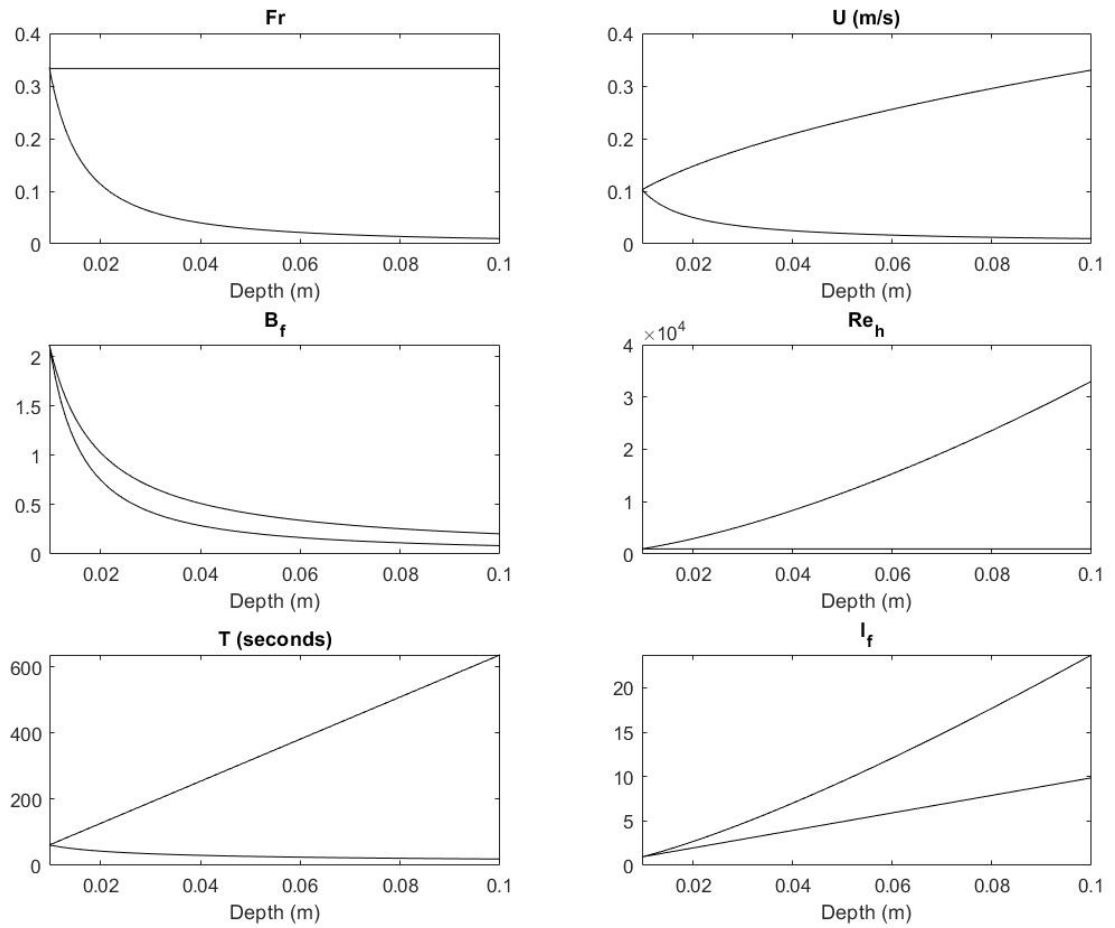
84

Figure 6.1: Parameter space with $W = 0.7$m and $K_w = 0.11$

7.   REFERENCES

Adrian, R. J., Christensen, K. T., and Liu, Z. C. (2000). "Analysis and interpretation of instantaneous turbulent velocity fields." Experiments in Fluids 29(3): 275-290.

ASTM E1300-16, "Standard Practice for Determining Load Resistance of Glass in Buildings," ASTM International, West Conshohocken, PA, 2016, www.astm.org

Bryant, Duncan B., et al. "Formation of Tidal Starting-Jet Vortices through Idealized Barotropic Inlets with Finite Length." Environmental Fluid Mechanics, vol. 12, no. 4, 2012, pp. 301-319., doi:10.1007/s10652-012-9237-4.

Carmer, Carl Friedrich v. "Shallow Turbulent Wake Flows Momentum and Mass Transfer Due to Large-Scale Coherent Vortical Structures." Karlsruhe, 2005.

Dean, Robert George, and Robert A. Dalrymple. Water Wave Mechanics for Engineers and Scientists. World Scientific, 1995.

Ghidaoui, M. S., et al. (2006), Linear and nonlinear analysis of shallow wakes, J. Fluid Mech., 548, 309-340.

Hassan, Anita, et al. "Texas City Dike Closed after Barge and Ship Collide."Houston Chronicle, Houston Chronicle, 24 Mar. 2014, www.chron.com/news/houston-texas/houston/article/Texas-City-dike-closed-after-barge-and-ship-5341213.php

Hutschenreuter, K., "Comparison of Laboratory PIV Analysis of Vortex Dynamics for Shallow Tidal Inlets with Results Using the Fine Resolution HydroDynamic Model," Masters thesis, Texas AM University.

Hutschenreuter, Katie L., et al. "Simulation of Laboratory Experiments for Vortex Dynamics at Shallow Tidal Inlets Using the Fine Resolution Environmental Hydrodynamics (Frehd) Model." Environmental Fluid Mechanics, 2019, doi:10.1007/s10652-019-09668-y.

Kashiwai, Makoto. "Tidal Residual Circulation Produced by a Tidal Vortex." Journal of the Oceanographical Society of Japan, vol. 40, no. 4, 1984, pp. 279-294., doi:10.1007/bf02302521.

Pizer, S. M.; Amburn, E. P.; Austin, J. D.; Cromartie, R.; Geselowitz, A.; Greer, T.; ter Haar

Romeny, B.; Zimmerman, J. B. Zuiderveld, K. (1987): Adaptive histogram equalization and its variations. Computer Vision, Graphics, and Image Processing 39(3): 355-368.

Roure, Francisco Nicolau Del, et al. "Structure and Evolution of Tidal Starting Jet Vortices at Idealized Barotropic Inlets." Journal of Geophysical Research, vol. 114, no. C5, 2009, doi:10.1029/2008jc004997.

Schlichting, Hermann (1979). Boundary-Layer Theory, 7th ed., McGraw Hill, New York, U.S.A.

Shavit, U.; Lowe, R. Steinbuck, J. (2007): Intensity Capping: a simple method to improve cross-correlation PIV results. Experiments in Fluids 42(2): 225-240.

Stamhuis, Eize J., and John J. Videler. "QUANTITATIVE FLOW ANALYSIS AROUND AQUATIC ANIMALS USING LASER SHEET PARTICLE IMAGE VELOCIMETRY." The Journal of Experimental Biology, 10 Oct. 1994.

Swamee, P.K., and A.K. Jain (1976). "Explicit Equations for Pipe Flow Problems." Journal of Hydraulic Engineering, ASCE, 1976, pp. 657-664.

Thielicke, W. and Stamhuis, E. J. (2014): PIVlab Time-Resolved Digital Particle Image Velocimetry Tool for MATLAB. http://dx.doi.org/10.6084/m9.figshare.1092508

Thielicke, W. and Stamhuis, E.J. (2014): PIVlab Towards User-friendly, Affordable and Accurate Digital Particle Image Velocimetry in MATLAB. Journal of Open Research Software 2(1):e30, DOI: http://dx.doi.org/10.5334/jors.bl

Thielicke, W. (2014): The Flapping Flight of Birds - Analysis and Application. Phd thesis, Rijksuniversiteit Groningen. http://irs.ub.rug.nl/ppn/382783069

Weitbrecht, V., et al. "Large Scale PIV-Measurements at the Surface of Shallow Water Flows." Flow Measurement and Instrumentation, vol. 13, no. 5-6, 2002, pp. 237-245., doi:10.1016/s0955-5986(02)00059-6.

Wells, M. G., and G. J. F. van Heijst (2003), A model of tidal flushing of an estuary by dipole formation, Dyn. Atmos. Oceans, 37(3), 223-244.

Westerweel, Jerry, and Fulvio Scarano. "Universal Outlier Detection for PIV Data." Experiments in Fluids, vol. 39, no. 6, 2005, pp. 1096-1100., doi:10.1007/s00348-005-0016-6.

Whilden, Kerri Ann, et al. "Investigation of Tidal Exchange and the Formation of Tidal Vortices at Aransas Pass, Texas, USA." 2015.

Whilden, Kerri Ann. "LABORATORY ANALYSIS OF VORTEX DYNAMICS FOR SHALLOW TIDAL INLETS." Texas AM University - College Station,Texas AM University, 2009.

White, Frank M. Fluid Mechanics. McGraw-Hill, 2011.